THE UNIVERSITY OF CHICAGO

DYNAMICS OF THE RANDOM FIELD ISING MODEL

A DISSERTATION SUBMITTED TO
THE FACULTY OF THE DIVISION OF THE PHYSICAL SCIENCES
IN CANDIDACY FOR THE DEGREE OF
DOCTOR OF PHILOSOPHY

DEPARTMENT OF PHYSICS

BY

JIAN XU

CHICAGO, ILLINOIS
AUGUST 2017

CONTENTS

LIST OF FIGURES

ACKNOWLEDGMENTS

First of all, I'd like to express my sincerest gratitude to my PhD advisor Tom Rosenbaum, for his continuously support of my research and study. Tom always motivate me to think logically, precisely, and scientifically. In good or bad day, he always encourage me. He also taught me working in parallel which benefit me throughout the research.

My sincere thanks also go to Daniel Silevitch. He is the best lab manager I've ever seen and also a good labmate. During our transfer from Chicago to Caltech, we worked through the toughest time and managed to built up a new lab at sub-basement of the Sloan building. I learned to be thorough and patient from him.

I'd also like to thank my thesis committee, Stephen Meyer, David Schuster, and Paul Wiegmann who provided me with the opportunities to go through committee meetings and the final defense.

I thank my fellow labmates in this lab. I benefit from the fruitful discussions with you guys. I thank Nayoon Woo, Alex Palmer, Yishu Wang, and Spencer Tomarken. I thank our collaborators especially Karin Dahmen from UIUC. Our $Nd_2Fe_{14}B$ experiment matches beautifully with your RG theory and there are more to expect with the $LiHo_xY_{1-x}F_4$ system. I also thank my friends Yifan Wang, Qiti Guo, Justin Jureller, former legendary machinist Helmut, present machinist Luigi Mazzenga from UChicago and Aaron Chew, Steve Carton, machinist John Van Seusen from Caltech.

Finally, I'd also like to thank my parents for their continuously supports. Special thanks to my wife Xi Lu. I'm lucky to have you by my side from Chicago to Pasadena.

ABSTRACT

The Random Field Ising Model (RFIM) is a general tool to study disordered systems. Crackling noise is generated when disordered systems are driven by external forces, spanning a broad range of sizes. Systems with different microscopic structures such as disordered magnets and Earth's crust have been studied under the RFIM. In this thesis, we investigated the domain dynamics and critical behavior in two dipole-coupled Ising ferromagnets $Nd_2Fe_{14}B$ and $LiHo_xY_{1-x}F_4$. With T_c well above room temperature, $Nd_2Fe_{14}B$ has shown reversible disorder when exposed to an external transverse field and crosses between two universality classes in the strong and weak disorder limits. Besides tunable disorder, $LiHo_xY_{1-x}F_4$ has shown quantum tunneling effects arising from quantum fluctuations, providing another mechanism for domain reversal. Universality within and beyond power law dependence on avalanche size and energy were studied in $LiHo_{0.65}Y_{0.35}F_4$.

CHAPTER 1

INTRODUCTION

Most physical and biological systems are disordered, even though the majority of theoretical models treat disorder as a weak perturbation. In this thesis we focus on the simple example of the Ising ferromagnet, where the Curie temperature is suppressed by the addition of disorder. The disorder is from chemical substitution of magnetic Ho^{3+} using non-magnetic Y^{3+} in $LiHo_xY_{1-x}F_4$ and the random packing of $Nd_2Fe_{14}B$ crystallites to form an uniaxially aligned bulk sample. The disorder is not sufficient to eliminate the ferromagnetism, but it controls a number of key magnetic properties[1].

1.1 Introduction to random field Ising model

The Random Field Ising Model (RFIM) has been studied extensively as a general model for the effects of disorder. In the RFIM, the standard Ising Hamiltonian is modified by adding an applied field along the Ising axis whose value varies randomly from site to site:

$$H = -\sum_{ij} J_{ij}\sigma_i^z\sigma_j^z + \sum_i h_i\sigma_i^z \tag{1.1}$$

where h_i is a site-random field and J_{ij} is the interspin interaction (spin exchange interaction, dipolar interaction, etc.). While the Hamiltonian can be modeled numerically, experimental realizations require finding materials for which the RFIM is an appropriate abstract description of the underlying microscopic Hamiltonian. The original experimental studies of the RFIM followed a proposal by Imry and Ma[2], in which a site-diluted Ising antiferromagnet in a large static magnetic field forms a realization of the RFIM Hamiltonian. While this approach proved fruitful for studying quantities such as the thermodynamic critical exponents[3, 4] and correlation lengths[5], the lack of a net long wavelength moment in antiferromagnets limits the potential probes and hence the set of physical questions that can

be addressed. Uniaxial relaxor ferroelectrics were subsequently shown to be realizations of the RFIM [6, 7] and similarly have provided insights into the critical and scaling behavior. Within the last decade, it has been shown that dilute dipole-coupled ferromagnets also can exhibit RFIM behavior. They arise when diluted, dipole-coupled Ising materials are placed in a static magnetic field applied transverse to the Ising axis. The combination of the off-diagonal elements of the dipole-dipole potential and the symmetry breaking of the disorder lets the uniform transverse field generate an effective site-random longitudinal field[8–10]. The initial realizations, first in the rare-earth fluoride $LiHo_xY_{1-x}F_4$[1, 8, 9, 11] and subsequently in the molecular magnet Mn_{12-ac} [10, 12], used dipole-coupled single spins. Both materials exhibit magnetic ordering at cryogenic temperatures due to the low energies of the dipolar coupling. Recently, Tomarken et al. demonstrated [13]that a sintered block of the rare-earth ferromagnet $Nd_2Fe_{14}B$ acts as a realization of the RFIM at room temperature, and that by tuning the strength of the disorder via an applied transverse field, the domain reversal energetics and hence the macroscopic hysteresis loop, can be varied at fixed temperature. In $Nd_2Fe_{14}B$, individual spins are exchange-coupled and form elongated domains due to the inherent crystalline anisotropy[14, 15]. The dominant reversal mechanism of the individual domains shifts between nucleation and wall-pinning depending on the temperature and the precise microstructure of the material[16]. These domains then interact via a dipolar coupling. The extended nature of the dipoles gives them much larger moments ($\sim 10^9$ Bohr magnetons) than individual spins would have, with a correspondingly higher energy scale (e.g. the Curie temperature for sintered $Nd_2Fe_{14}B$ is 585 K[17]).

Traditionally, disorder in bulk materials can't be tuned easily. For example, thin-film magnetic materials, in the as-grown state, form a disordered granular array on top of the substrate whose morphology and degree of disorder can be controlled by varying the deposition conditions such as background sputtering pressure and deposition rate[18, 19]. Once the samples are grown the disorder can be reduced by heat treatment. This not only pro-

duces variations in the local potentials but also limits the application. Thin-film magnetic materials experiencing strong shape anisotropy effects such as Co/Pt are often used as media for information storage. The bit is stored in the state of the local magnetic domains. The information storage process is a result of the competition between the disorder's tendency to pin the bit and thermal fluctuations, and the magnetic field to flip it. In practice, the local magnetic domains are often heated to reduce the coercivity while writing and cooled while reading[20]. The freedom to continuously tune the disorder allows for another way to adjust the competition and thus has potential applications[21–23].

1.2 Dipole-coupled disordered ferromagnet

In this section I will discuss the origin of the effective random field in a disordered, dipole-coupled Ising ferromagnet. The two systems that we studied, $LiHo_{0.65}Y_{0.35}F_4$ and $Nd_2Fe_{14}B$, both have a ground state Ising doublet. The interactions between spins in $LiHo_{0.65}Y_{0.35}F_4$ and grains in $Nd_2Fe_{14}B$ are dipolar coupled. The source of disorder and dipolar energy scales are very different between the two, but that doesn't affect the fundamental physics. To that end, I will focus the discussion on $LiHo_{0.65}Y_{0.35}F_4$. Pure $LiHoF_4$ is a dipole-coupled magnet with its magnetism carried by the Ho^{3+} ions. As indicated in Fig. 1.1, it carries large magnetic moments strongly aligned along the c axis of the tetragonal lattice and coupled to each other mainly via the dipolar interaction[24].

At high temperature $LiHoF_4$ is a paramagnet with a second-order phase transition into the ferromagnetic state at $T_c = 1.53$ K[25]. With a transverse field relative to the Ising axis, the system is a realization of the transverse field Ising model with a continuous phase boundary between the Ht = 0 at T_c and Ht = 50 kOe at zero temperature [26], as indicated in Fig. 1.2. The ground state of the Ho^{3+} ion in the crystal field is a doublet and the first excited state is at T = 9.4 K. At temperatures much lower than 10 K, only the ground state doublet is significantly populated, denoted as $\langle\uparrow|$ and $\langle\downarrow|$. The z-component angular

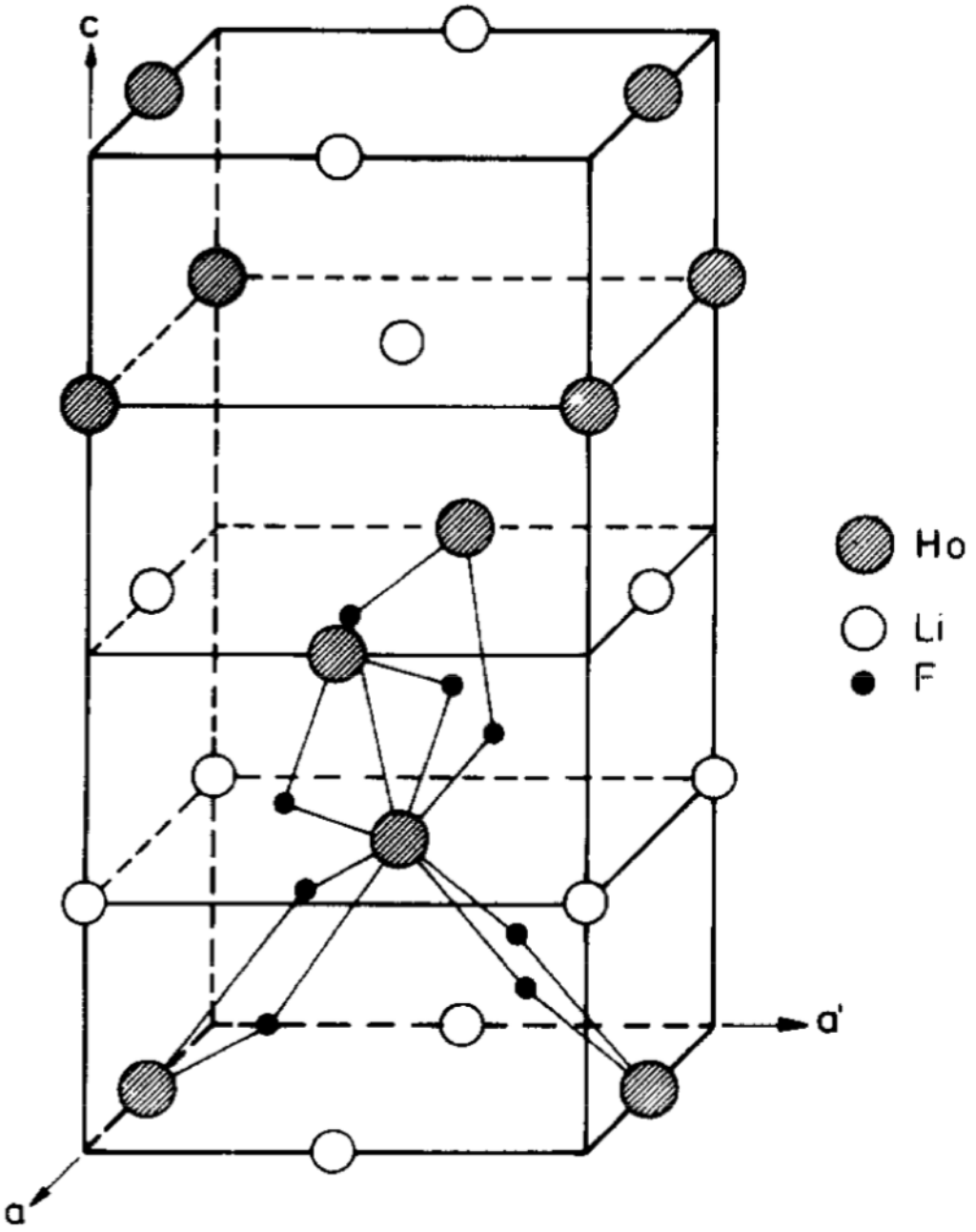

Figure 1.1: Schematic representation of the unit cell of pure $LiHoF_4$. Chemical substitution of Ho^{3+} using Y^{3+} forms $LiHo_xY_{1-x}F_4$. This figure is from Ref. [24]
.

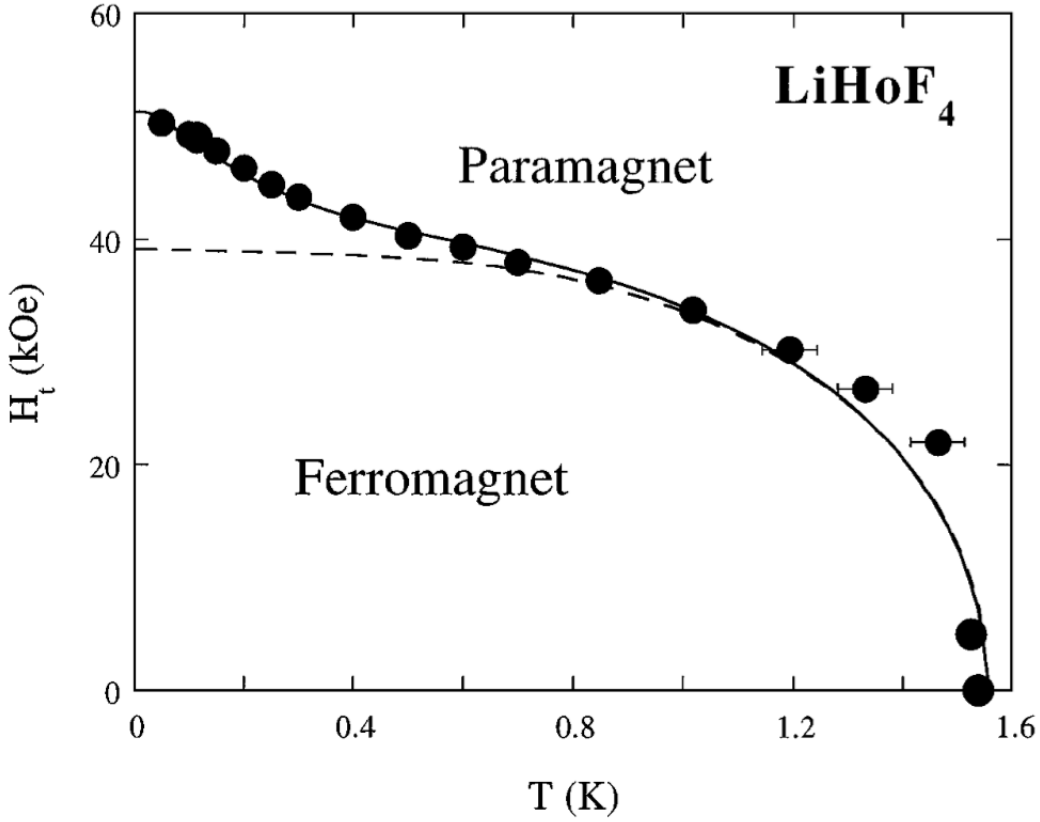

Figure 1.2: Experimental phase boundary (filled circles) for the pure $LiHoF_4$. Dashed line is a mean-field theory including only the electronic spin while sold line is the boundary includes hyperfine interaction. From Ref. [26]

.

momentum thus satisfies $\langle\uparrow|J^z|\uparrow\rangle = -\langle\downarrow|J^z|\downarrow\rangle$ andJ^x and J^y have zero expectation value in ground-states space[27]. This system thus shows strong Ising anisotropy of the ground state. For concentrations above $x \sim 0.3$ and at zero transverse field, the $LiHo_xY_{1-x}F_4$ system remains ferromagnetic, where T_c follows the mean field theory prediction $T_c(\mathrm{x}) = \mathrm{xTc}$. In finite transverse field, T_c is suppressed below the mean-field expectation due to the presence of effective random fields arising from the dilution-induced disorder.

1.3 The origin of the effective random field

There are five main components of the Hamiltonian: the crystal field, the transverse field, the dipolar interaction, the spin-exchange interaction between each site and its nearest neighbors, and the hyperfine interaction[27]. Since a single Ho^{3+} ion in the crystal has a tightly bound $4f$ electronic structure, this results in very small wave-function overlaps between neighbors[28]. So the nearest-neighbor exchange interaction (0.34 K) is much smaller compared to the dipolar interaction ($\sim 1K$). The hyperfine interaction is small, entering below T = 0.4 K, and not germane to the context of this thesis. So we neglect the exchange interaction and the hyperfine interaction for the following discussion. We use B_x for transverse field to emphasize its crystalline direction in the following discussion. The Hamiltonian is then:

$$H = -\sum_i H_{crystal}(J_i) - g_L\mu_B \sum_i B_x J_i^x + \frac{1}{2}(g_L\mu_B)^2 \sum_{ij} D_{ij}^{\alpha\beta} J_i^\alpha J_j^\beta \qquad (1.2)$$

where g_L is the Lande g factor, μ_B is the Bohr magneton, the dipolar term $D_{ij}^{\alpha\beta}$ depends on the relative position of all the spins, and $\alpha, \beta = x, y, z$. For the true ground state, $\alpha, \beta = z$ where $D_{ij}^{zz} = \frac{r_{ij}^2 - 3z_{ij}^2}{r_{ij}^5}$, z_{ij} is the relative distance of two spins, and is the longitudinal distance.

1.3.1 Quantum fluctuations induced by the transverse field

When the transverse field is presented, it mixes the degenerate ground state with the higher-level crystal-field states[27, 29]. This is illustrated in Fig. 1.3. The first two terms of the Hamiltonian H can be rewritten as $\sum_i \left[\frac{1}{2}\big(E_i^1 + E_i^2\big) - \frac{1}{2}\big(E_i^1 - E_i^2\big)\sigma^x\right]$, where E_i^1 and E_i^2 are the Eigen-energy of states at site i. This is done by mapping J_i^x onto a two-dimensional Hilbert space $\langle 1|$ and $\langle 2|$, where $\langle 1|$ is spin-left $\langle \leftarrow|$ (same direction as B_x) and $\langle \rightarrow|$ is spin-right. Both energies are a function of transverse field B_x. So it can be rewritten as $\sum_i \left[E_i\big(B_x\big) - \Delta\big(B_x\big)\sigma^x\right]$. Effectively, the degenerate energy splitting can be interpreted as

an effective magnetic field on a s-1/2 system at each site [27].

1.3.2 The origin of the effective random field

For the dipolar term we map it onto the basis of a two-dimensional unit matrix and three Pauli spin matrices $J_\alpha = C_\alpha + \sum_\beta C_{\alpha\beta}\sigma^\alpha$ where the coefficients $C_{\alpha\beta} = C_{\alpha\beta}(B_x)$. Again, the dipolar interaction coefficients explicitly rely on the strength of the transverse field B_x. Using this representation, the off-diagonal Hamiltonian, $H_{zx} = \frac{1}{2}\big(g_L\mu_B\big)^2 \sum_{i,j} D_{ij}^{zx} J_i^z J_j^x$, is composed of a series of terms such as σ_i^z, $\sigma_i^z\sigma_j^x$, $\sigma_i^z\sigma_j^z$, etc. The largest component is $\big(C_{zz}B\big(x\big)\big)^2 D_{ij}^{zx}\sigma_i^z\sigma_j^x$, which is two orders of magnitude larger than the rest of them [27]. The effective Hamiltonian becomes:

$$H = -\sum_{ij} J_{ij}\sigma_i^z\sigma_j^z - \Gamma\sum_i \sigma_i^x \tag{1.3}$$

where J_{ij} is the general pairwise spin interaction and Γ denotes the transverse magnetic field with its accompanying quantum fluctuations [1]. $\Gamma = \Delta(B_x)$ where $\Delta(B_x)$ is the energy gap between the two originally degenerate ground states. Hence Γ sets the quantum tunneling rate [1]. In pure samples, the first term has no off-diagonal dipolar interaction because the off-diagonal term $D_{ij}^{\alpha\neq\beta}$ is cancelled by symmetry. When the Ho^{3+} ions are partially substituted by non-magnetic Y^{3+}, as for example in the $LiHo_{0.65}Y_{0.35}F_4$ crystals that I am studying, this translational symmetry no longer holds [9]. The $-\sum_{ij} J_{ij}\sigma_i^z\sigma_j^z$ term implicitly is a function of transverse field B_x . Using second-order perturbation theory, the effective random field $\Gamma \propto B_x^2$ for small B_x [27] .The transverse field B_x, the broken symmetry from the dilution, and the off-diagonal term $D_{ij}^{\alpha\neq\beta}$ combine to lead to a net random field on each site. Missing any of these conditions would result in zero effective random field. As shown in Fig. 1.4, the central spin in the diluted lattice feels a net effective random field due to symmetry breaking while the central spin in the undiluted one doesn't. (Following [11]).

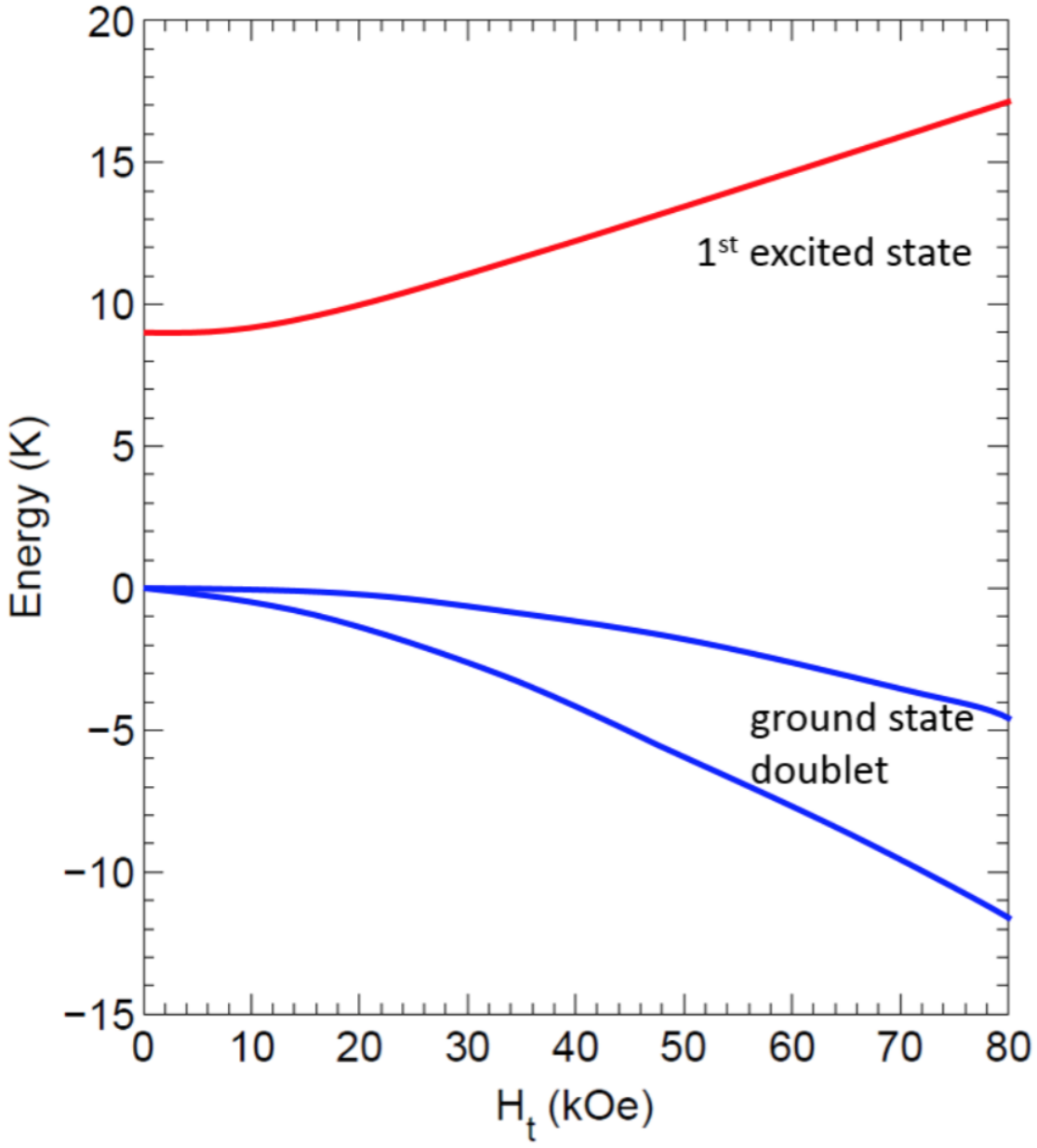

Figure 1.3: Ground states doublet and the first excited energy diagram with the application of a transverse magnetic field. From Ref. [29]

.

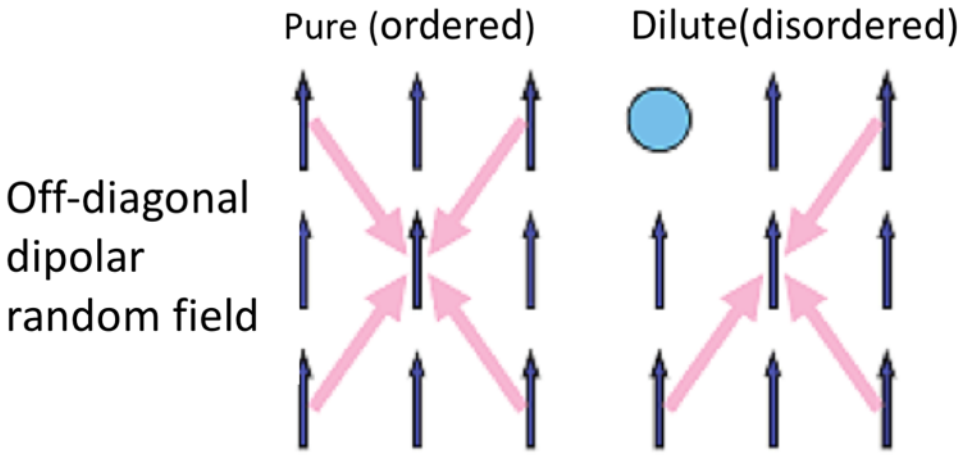

Figure 1.4: Physics picture of dipole-coupled disordered Ising ferromagnet where off-diagonal terms of the dipole interaction act to enable the random fields. Left panel shows undiluted system where the off-diagonal matrices cancel due to symmetry. Right panel shows the broken symmetry where the effective local longitudinal field arises due to a nonzero off-diagonal dipolar term $\sum_i D_{ij}^{zx}$ for site j
. From Ref. [11].

The thesis is organized as follows. Chapter 1 describes the features of the Random Field Ising Model in ferromagnetic materials. Chapter 2 presents the methods which we employed to collect and analyze the data. Chapter 3 describes the physical realization of the random field Ising model in the room temperature ferromagnet, $Nd_2Fe_{14}B$. Chapter 4 continues the study of this model system with dynamical characterization of domain reversal and critical exponents in $Nd_2Fe_{14}B$. Chapter 5 reports results of Barkhausen noise measurements in the low-temperature, dipolar-coupled Ising ferromagnet $LiHo_{0.65}Y_{0.35}F_4$, and discusses possible universality beyond the power law analysis. Chapter 6 summarizes the results of the thesis and suggests follow-on experiments.

CHAPTER 2

METHODS

The response of a ferromagnet to a time varying magnetic field has been studied extensively via experiment, numerical modeling, and theory. The magnetization, rather than evolving continuously as the field changes, often increments in discrete steps as individual domains or sets of domains rapidly switch direction. Fig. 2.1(a) shows the hysteresis loop for $Nd_2Fe_{14}B$ at T = 150 K. The zoom-in shows discrete steps in the M-H curve as the longitudinal field is ramping. These steps were observed as voltage pulses in inductive pickup coils wrapped around the magnet, picking up the change in magnetization versus time, $\frac{dM}{dt}$. The crackling noise arising from the superposition of many such pulses is known as Barkhausen noise [30]. Detailed measurements of the spectrum of this noise provide a sensitive probe of the internal energetics of domain reversal [31], and the effects of variable disorder.

2.1 Barkhausen noise detection for $Nd_2Fe_{14}B$

We measured the static magnetization of 2 mm diameter by 10 mm length cylinders of commercially sintered $Nd_2Fe_{14}B$ via Hall magnetometry, using a pair of passive GaAs Hall sensors (Toshiba THS118) in a gradiometric configuration to remove the contribution of the applied field to the Hall signal. The easy axes of the samples were oriented parallel to the cylindrical axis. A 320 turn pickup coil was wrapped around the same $Nd_2Fe_{14}B$ cylinders and an identical-geometry, empty coil wired in opposition to cancel the $\frac{dH}{dt}$ from the applied field. The signal was amplified by a factor of 10,000 with a Stanford Research SR560 low-noise voltage preamplifier, followed by a 120 kHz Krohn-Hite 3988 low-pass filter to eliminate aliasing effects, and finally a National Instruments USB-6211 250 kHz/16 bit digitizer. To avoid 60 Hz and its harmonics (mainly 3rd order), the pre-amp operated on battery mode. Longitudinal and transverse magnetic fields were supplied by a dual axis 5

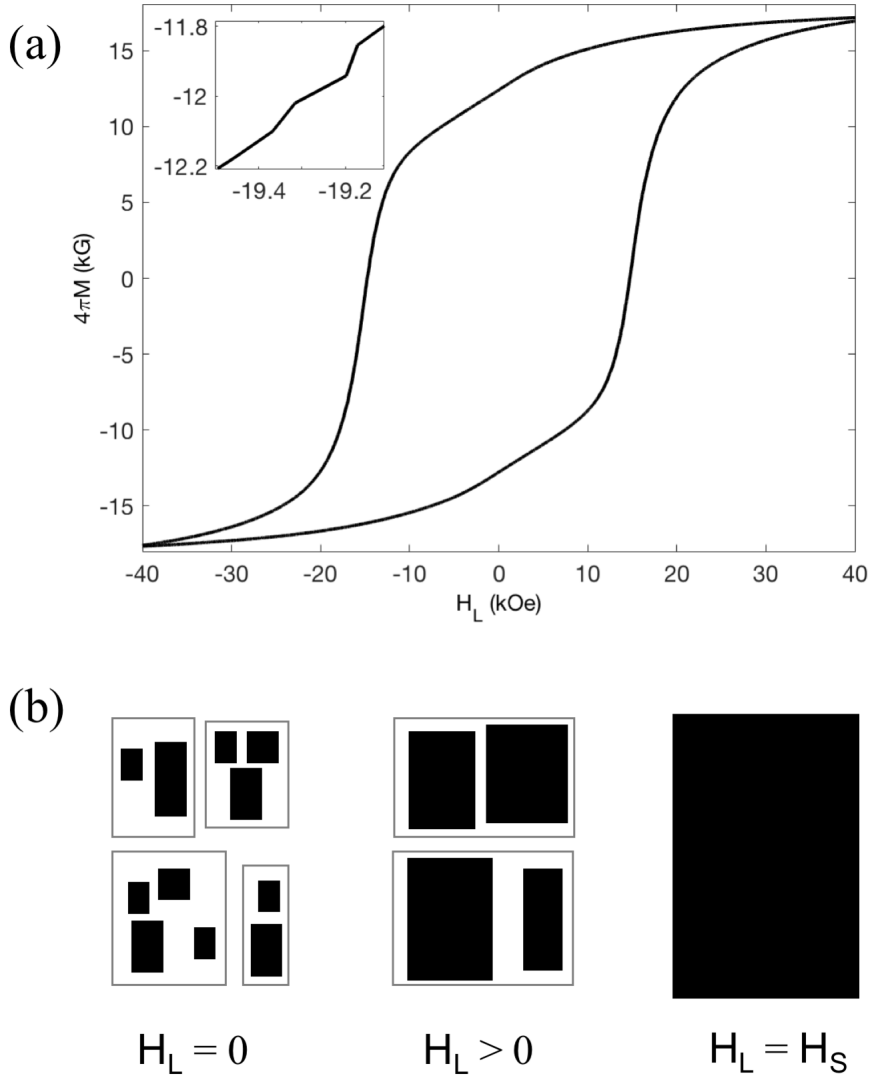

Figure 2.1: Overview of Barkhausen noise measurements. (a) Hysteresis loop of $Nd_2Fe_{14}B$ at T = 150 K. Inset is the zoom-in of the steepest regime of the M-H curve. (b) Schematic of domain flips as longitudinal field is ramping and induced voltage. As the longitudinal field increases, coarsening effects increase the average size of the magnetic domains, which can span several structural grains and can average out the intergrain disorder. When the longitudinal field reaches saturation field H_S, all the magnetic domains coalesce as one and align along the Ising axis.

T/2 T superconducting magnet. Hysteresis loops were typically obtained with the transverse field fixed and the longitudinal field ramped at a constant 0.4 T/min between ± 4.5 T. In order to verify that the field ramp rate was in the adiabatic limit, data at T = 4.2 K was collected at a ramp rate nearly an order of magnitude slower, 0.05 T/min. No difference was observed in the values found for the exponents within the statistical error bars. As shown in Fig. 2.2, the energy event histograms for 0.4 T/min and 0.05 T/min ramp rates at T = 4.3 K and $H_T = 0$ are visually very similar, and the values for the fitted power law exponents are the same to within the experimental uncertainty. It is important to note that even the faster ramp rate is very slow by the standards of typical Barkhausen measurements. Most Barkhausen experiments take seconds to tens of seconds to complete a hysteresis loop, whereas even the faster ramp rate in our measurements requires nearly an hour to complete a loop. Given the large field scales involved, it was not necessary to screen out the Earth magnetic field. For each temperature/transverse field point investigated, a series of hysteresis loops was measured to obtain a minimum of 106 events; depending on temperature and field, this required 25 to 38 loops. For measurements at T = 4.2 K, helium exchange gas was used to place the sample in thermal contact with the liquid helium bath; at T = 150 and 300 K, the sample was in vacuum and a PID loop was used to stabilize the temperature.

2.2 Barkhausen noise detection for $\mathbf{LiHo_{0.65}Y_{0.35}F_4}$

The Barkhausen noise was measured in an Oxford Instruments Kelvinox MX400 Helium dilution refrigerator with base temperature of 10 mK. The dilution refrigerator and other data-taking instruments were inside a shielded room. The data is transmitted through a fiber bridge and USB extension cords to the computer outside the shielded room. The sample dimensions were 10 mm x 5 mm x 5 mm. The sample was heat sunk by four pieces of 0.027-inch-thick sapphire plates. The sapphire plates were attached onto copper wires via silver epoxy and screwed into the cold finger. Both ends of the copper wires were stripped and

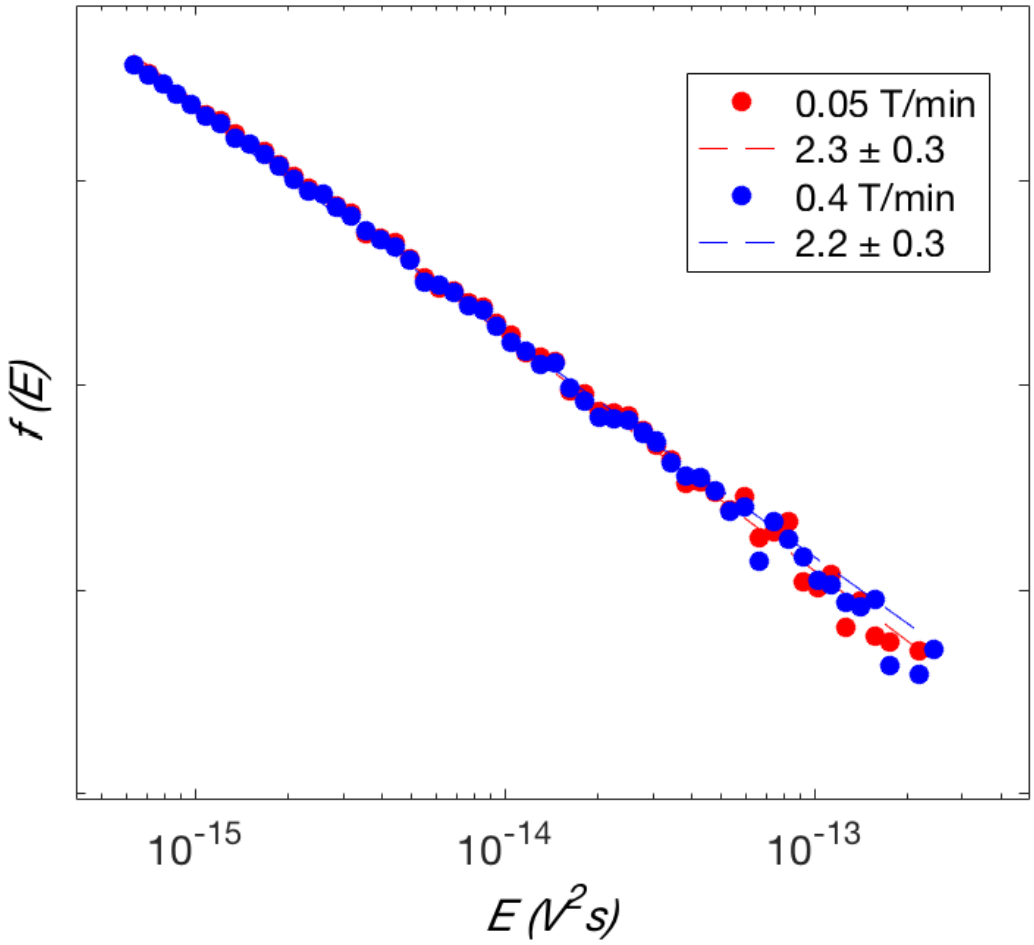

Figure 2.2: Probability distribution of avalanche energy for for 4 and 0.5 kOe per minute at T = 4.3 K and $H_T = 0$. The dashed lines are the power law fits for each curve. Their critical exponents are 2.2 and 2.3 respectively and are within experimental uncertainty.

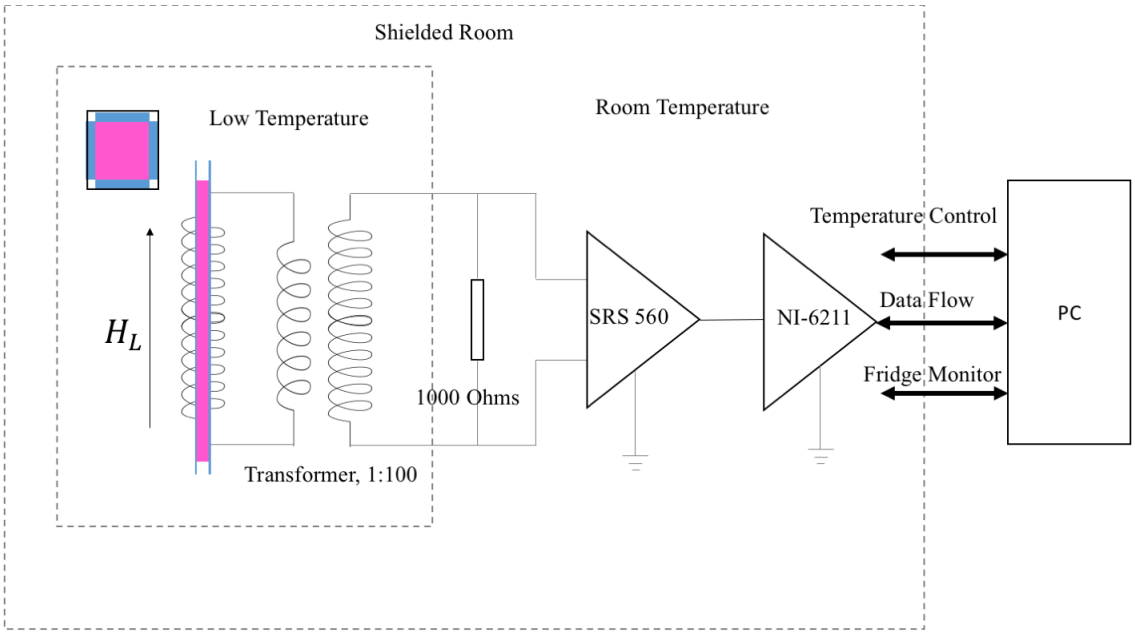

Figure 2.3: A schematic description for detecting Barkhausen noise in $LiHo_{0.65}Y_{0.35}F_4$. Upper left shows a cross-sectional view of the sample, the sapphire heat sinks, and the square coil.

squeezed into a flat surface to ensure good thermal contact. Insulating sapphire was chosen to eliminate eddy current heating due to the ramping of the magnetic field. The pickup coil is 150 turns and crafted to be square to improve the filling factor. The resonance frequency of the coil is about 1MHz, one order of magnitude higher than the audio frequency. The coil was wrapped around the center of the sample to avoid edge effects.

To improve the signal to noise ratio (SNR), we applied a two-stage amplification scheme (see Fig. 2.3). The signal was first amplified by an impedance matching cryogenic transformer (1:100). The Johnson noise of such a small resistance can be neglected. The working bandwidth is from 100 Hz to 100 kHz. A 1000 Ohm resistor was added to the circuit to ensure minimum signal reflection and best energy transfer. The signal then went to an SRS560 low noise preamp with differential and AC inputs for high common mode rejection ratio (CMRR) to avoid possible ground loop noise. For lowest effective noise, we used a gain of 2000 (see Fig. 2.6). The combined gain was 200,000. A 1 MHz low pass filter was applied to

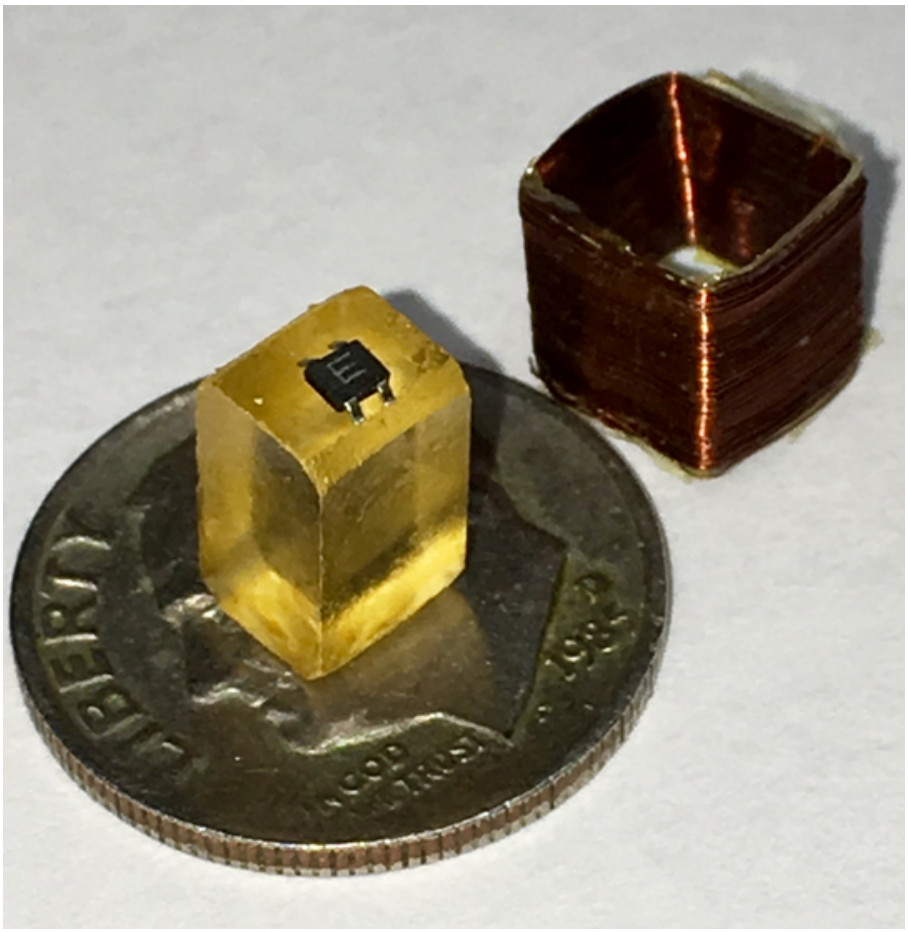

Figure 2.4: Photograph of single-crystal $LiHo_{0.65}Y_{0.35}F_4$ mounted on a GaAs Hall magnetometer. The Ising axis is parallel to the long axis of crystal. The pickup coil is on the right. Coin is for scale.

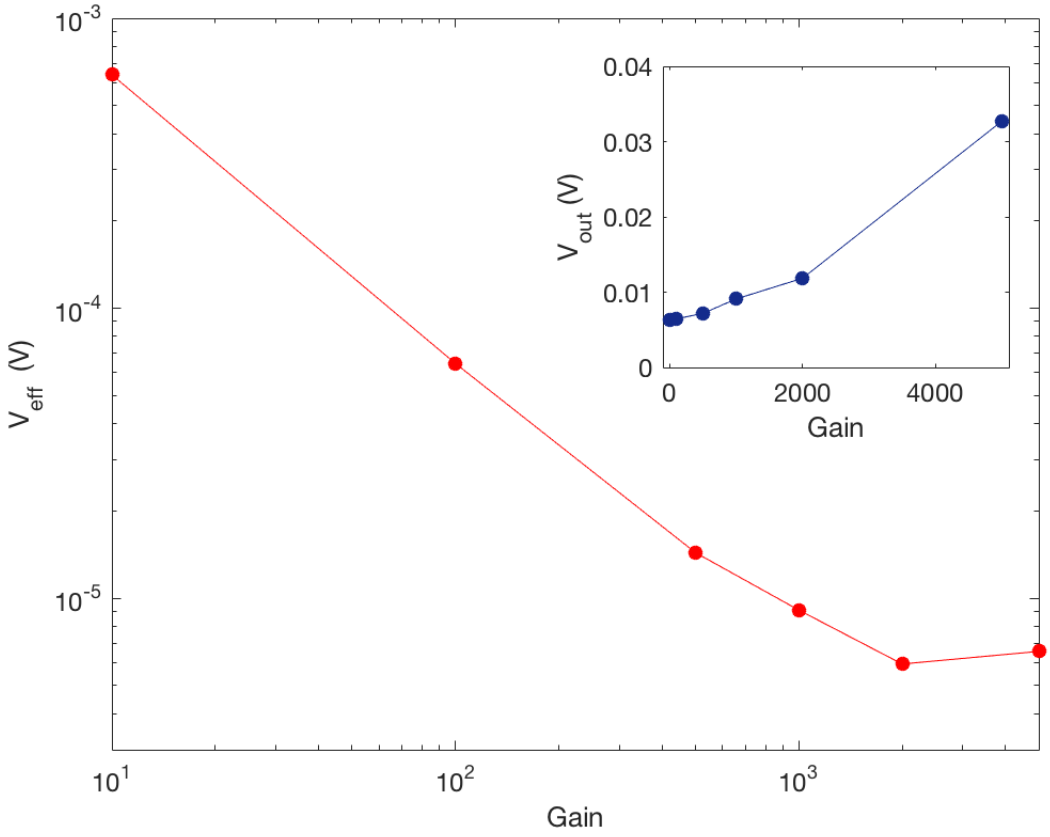

Figure 2.5: SRS560 Effective noise vs Gain. Effective noise is defined as the standard deviation of the noise divided by the gain. Inset is the raw noise floor vs the gain. We picked a gain of 2000 for the lowest effective noise.

reduce aliasing. The output signal of the preamp was sampled via a National Instruments USB-6211 250 kHz/16 bit digitizer and saved to the computer.

The longitudinal magnetic field was provided with a 2 inch 8T uniaxial superconducting magnet. The magnet was ramped at 0.08 T/min. Again, to verify that the field ramp rate was in the adiabatic limit, we collected data at a ramp rate of 0.01 T/min up to 0.12 T/min. No difference was observed in the values found for the averaged shape of the avalanches. We used the same GaAs magnetometers as in the $Nd_2Fe_{14}B$ experiments for magnetization measurements.

2.3 Data analysis

After data acquisition, a software 1.1 kHz high-pass filter was applied to the data to remove static offsets, external power-line noise, and other spurious low-frequency effects. For $Nd_2Fe_{14}B$ we followed the data analysis chain from [32] as the signal-to-noise ratio is relatively high. Since the noise floor follows closely a Gaussian distribution, individual events were identified by looking for voltages that deviated from the mean by more than 3.5 standard deviations of the time-independent background-voltage noise of the measurement chain. This threshold was chosen to maximize the number of accepted sample events while minimizing the rate of spurious events arising from amplifier or digitizer noise. The data was stored in binary format and each file contained 2^{18} points (for the Fast Fourier Transform).

The avalanche events in $LiHo_{0.65}Y_{0.35}F_4$ are two orders of magnitude smaller in magnitude than the events in $Nd_2Fe_{14}B$ because of the much smaller domains and their associated moments. To identify an event, we applied the following three steps. First, we define a threshold of 3.5 sigma standard deviations above the noise floor. Then we search all the points above zero for an event. Once the points are mostly defined, we linearly extrapolate the data points to zero for a variable number of points until the intercepts on time axis converge.

We have collected about 1,000 events for each temperature at 80, 250, 500, 600, and 700 mK. The total volume of data is about 10 Terabytes. To handle the big data, we developed software based on MATLAB and PYTHON. The algorithms work as follows:

1. Let D_i denotes the ith data in one dataset (one hysteresis loop) and x_{ij} denotes the jth sample in D_j.

2. For j =1,2,...2^{18},

   (a) Search x_{ij} to x_{ij+5}. if all a_{ij+p} (p=0,1,...5) < 3.5*STD(D_i), stop searching,

   (b) Let d_{kj} be the kth cluster, 1<=k<=length(x_{ij}),

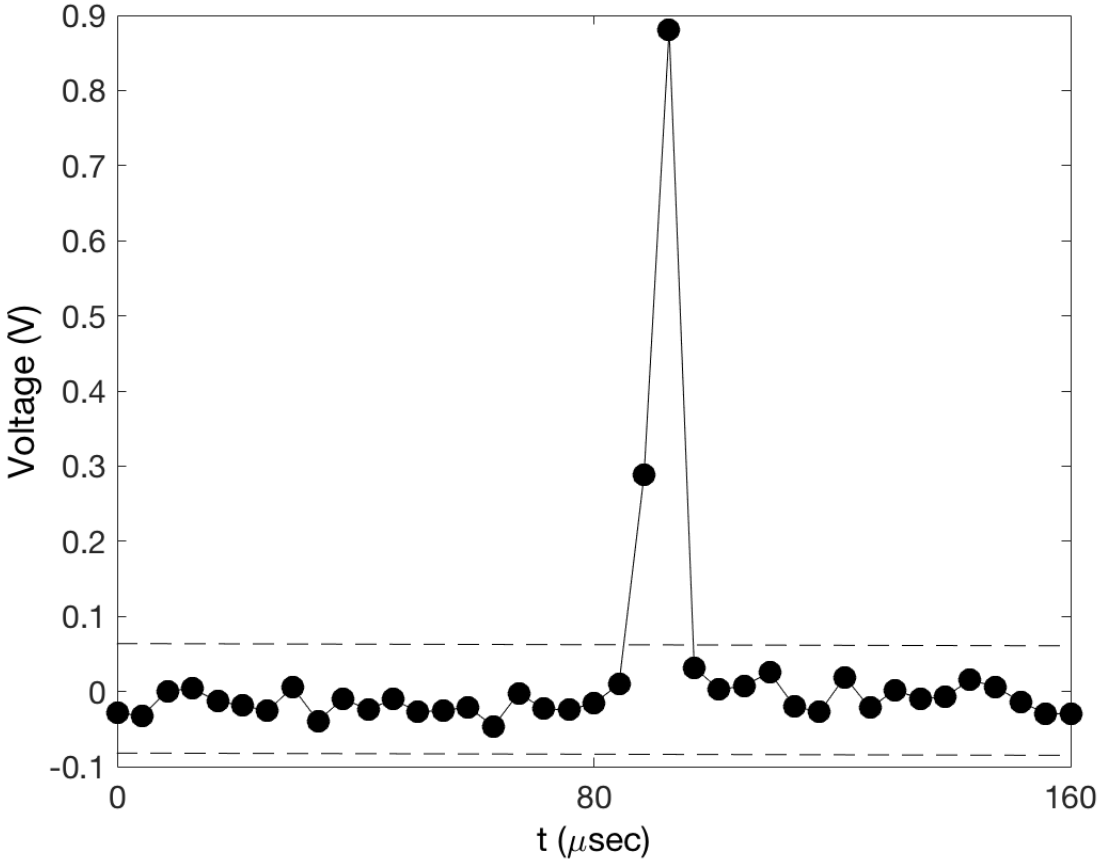

Figure 2.6: Time series of induced voltage on a pickup coil wrapped around a $Nd_2Fe_{14}B$ cylinder at T = 150 K showing the pulse structure over a duration of approximately 8 μs.

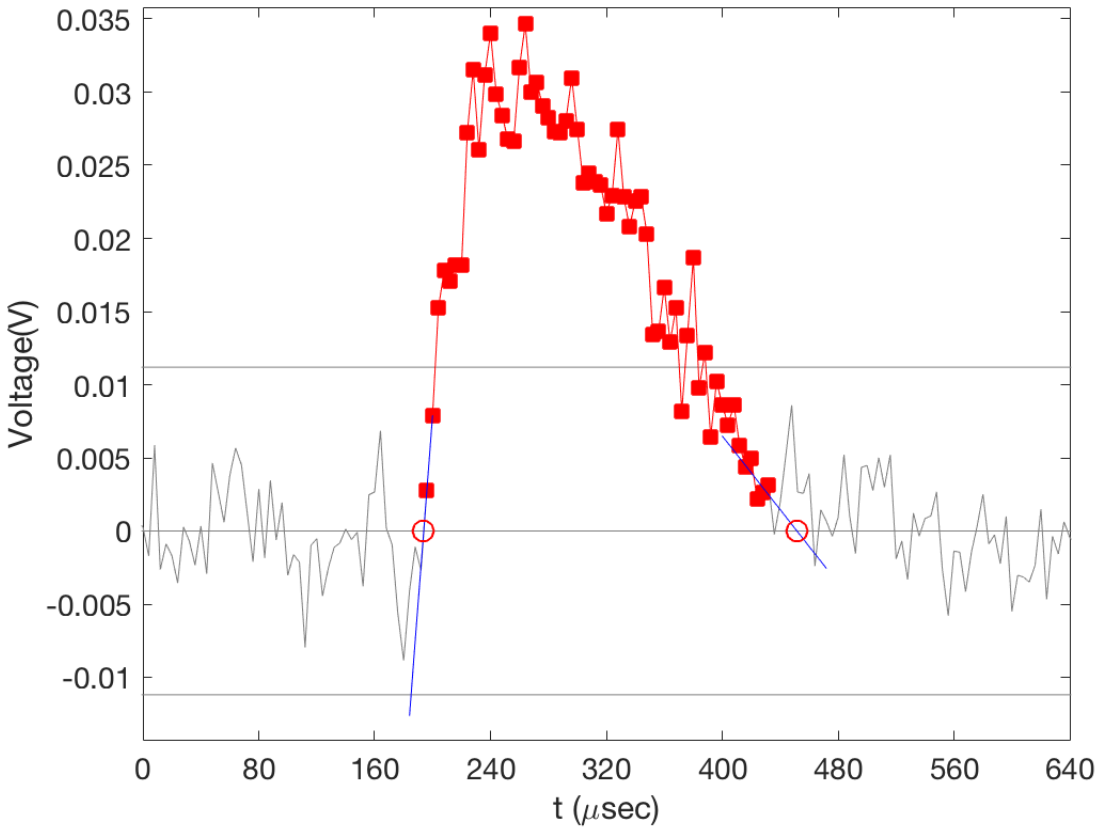

Figure 2.7: Time series of induced voltage on a pickup coil wrapped around the $LiHo_{0.65}Y_{0.35}F_4$ single crystal at T = 80 mK. The whole event is defined as the solid squares plus the (extrapolated) open circles. The blue line is the linear extrapolation to zero and the gray is the noise floor.

(c) Search all the neighbor points above zero for d_{kj},

(d) Let D_{kj} denotes the new cluster,

(e) Do dynamical linear extrapolation on D_{kj} until x-intercepts converges,

(f) Round the duration t_{ij} to the nearest integer count T_n and do linear interpolation,

CHAPTER 3

$Nd_2Fe_{14}B$: A RANDOM FIELD ISING FERROMAGNET AT ROOM TEMPERATURE

This Chapter is based on the published material in "Reversible Disorder in a Room Temperature Ferromagnet", S.L. Tomarken, D.M. Silevitch, G. Aeppli, B.A.W. Brinkman, J. Xu, K. A. Dahmen, and T.F. Rosenbaum, Advanced Functional Materials 24, 2986 (2014).

3.1 Introduction: The RFIM at room temperature

For more than 30 years, a host of different materials have been studied as experimental realizations of the field-tuned Random Field Ising Model (RFIM). The initial realizations, site-diluted antiferromagnets [21, 33] opened the door for extensive work on the critical behavior and dynamics [34, 35] of the RFIM, but the absence of a net moment limited the tools that could be applied. Within the last decade, it has been shown that dilute dipole-coupled ferromagnets also can exhibit RFIM behavior. The combination of off-diagonal components in the dipole-dipole coupling term and the breaking of translational invariance due to random dilution leads to an effective random field whose strength can be tuned continuously via a uniform magnetic field applied transverse to the Ising axis [1, 8, 9]. Experimental realizations have been observed in the dilute rare-earth fluoride $LiHo_xY_{1-x}F_4$ [11] and the molecular magnet Mn_{12-ac}. Unfortunately, both materials are only ferromagnetic at temperatures below 1 K due to the intrinsically small energy scale of the single-spin dipole-dipole coupling. For dipole-coupled ferromagnets to be stable at elevated temperatures, the individual dipoles must have moments two to three orders of magnitude larger than the single-ion moments of the Li(Ho,Y)F_4 or Mn_{12-ac} systems. We satisfy this fundamental constraint by considering a rare-earth ferromagnet, $Nd_2Fe_{14}B$, with high crystalline anisotropy and a tendency to form elongated grains, as illustrated in Fig. 3.1 [36].

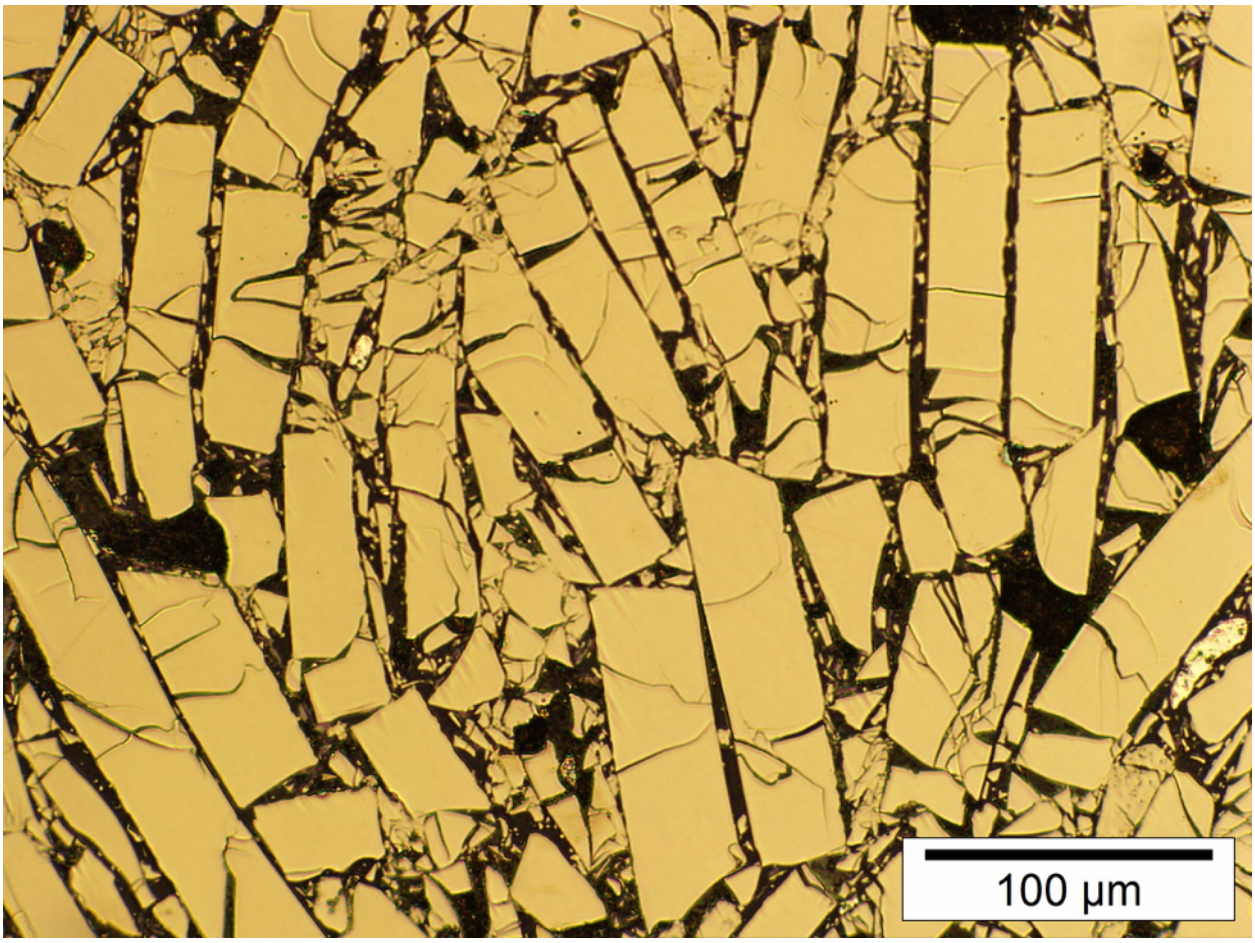

Figure 3.1: Optical image of a $Nd_2Fe_{14}B$ crystal at room temperature. The Ising axis is along the vertical direction.

3.2 Energy scales and general magnetic properties of $Nd_2Fe_{14}B$

The behavior of the magnet as a whole effectively separates into two length and energy scales: domains within a single grain and interactions between grains. At the smallest length scales, the individual spins are exchange-coupled, yielding a Curie temperature of $T_c = 585$ K [17]. At zero applied field they form domains whose size can be estimated from the known anisotropy energies and saturation magnetization to be of order $0.2-0.3\ \mu$m [37]. This yields a typical net moment of order 10^9 Bohr magnetons and an interdomain dipole interaction energy of approximately $5\ k_B$T at T = 300 K [16] Due to the crystalline and shape anisotropy [14, 15] each grain ultimately acts like a single effective spin that couples to nearby grains via the dipolar interaction (the long range nature of the dipole interaction results in a coupling that extends beyond nearest neighbors). While this energy scale is large compared to typical magnetic storage media, the results reported here represent a proof of concept that RFIM effects can be used to tune the behavior of room temperature ferromagnets. This ensemble of grains with typical size (50 mm $\times$ 15 mm $\times$ 15 mm) mimics the collection of individual dipoles in the previously studied RFIM materials and may be expected to exhibit comparable behavior. The large-scale grain structure can be imaged directly (Fig. 3.2(a), (b) insets). Optical imaging to reveal the shape of the large-scale granular structure followed polishing of the sample to an optical flat and decoration by depositing a commercial colloidal-suspension ferrofluid (Ferrotec EMG 308) and evaporating the liquid. The ferrofluid preferentially settles at the grain boundaries and enhances the contrast.

As can be seen from the two samples shown in Fig. 3.2, the grains are randomly packed in the material with the long axis of the majority of grains oriented parallel to the bulk easy axis of the sample (vertical in Fig. 3.2); Sample A contains approximately 60% elongated grains by volume and Sample B contains approximately 96%. This random packing is key to the observation of the RFIM, as the random distribution breaks the translational symmetry which otherwise would result in a net cancellation of the off-diagonal terms in

the dipole-dipole interaction tensor. Random packing of dipoles is known under some circumstances to destroy the long-range ordered state and instead create a glass state with no net magnetization [38]. However, the large remnant magnetization observed in this case (75% and 86% of M_s for $H_T = 0$ for samples A and B in Fig. 3.2(a) and (b), respectively) demonstrates that this sample has sufficiently high density and low frustration to support an ordered ferromagnetic state [39].

3.3 Pinning effects and broadening of the hysteresis loop

As a longitudinal field hl is applied and the magnetic domains are aligned, the effects of disorder and pinning change. Starting in the limit of high longitudinal field, defined when the magnet is near saturation, the average domain size approaches the dimensions of the sample. As sketched in Fig. 3.2, there are only a few, large domains due to the nearly uniform ordering of magnetic grains parallel to the applied field. With reduced longitudinal field, new domains nucleate within the material and the average domain size eventually becomes small compared to the typical grain size of order 10 μm [15]. During magnetization reversal, domain wall pinning occurs between the grains and material defects within the sample [38], fixed at fabrication. The number of such pinning sites a propagating domain wall encounters is proportional to the surface area of the wall; by contrast, the magnetization of the domain is proportional to the volume. Hence, at high longitudinal field, where there are a small number of big domains, the effective strength of the pinning is weaker than at low longitudinal field, where the higher surface area to volume ratio of the smaller domains results in stronger effective pinning.

We plot in the main panels of Fig. 3.2(a),(b) magnetic hysteresis loops for both samples as a function of hl beyond saturation ($\pm$25 kOe) at a series of constant transverse fields, H_T. The saturation magnetization in the longitudinal direction is only weakly dependent on H_T, decreasing by 3% (A) and 2% (B) at 7 kOe of transverse field and quantitatively

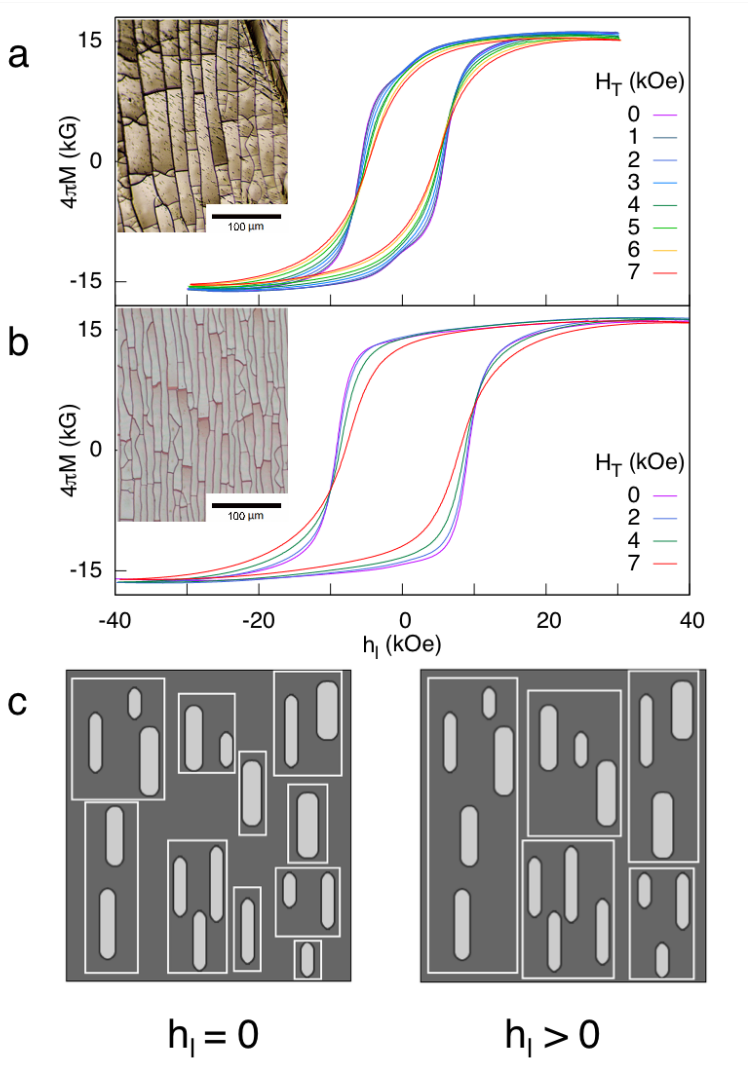

Figure 3.2: Overview of magnetic behavior of $Nd_2Fe_{14}B$. (a),(b). Magnetic behavior and structural morphology of two samples of $Nd_2Fe_{14}B$. Main panels: Magnetic hysteresis loops at T = 300 K for a series of transverse magnetic fields. Loops are swept out at a constant ramp of 0.75 kOe/min along the longitudinal (easy) axis while keeping the transverse field fixed. At low (high) longitudinal field, application of a transverse field narrows (broadens) the hysteresis. Insets: Optical micrographs of the $Nd_2Fe_{14}B$ samples grain structure using dried ferrofluid as a fine-powder contrast-enhancing agent that preferentially settles in the grain boundaries. The magnetic easy axis is in the vertical direction. (a). The granular structure is polydisperse in both size and aspect ratio, leading to a clear separation of the high and low field regimes. (b). The granular structure consists almost entirely of elongated aspect ratio grains, yielding a squarer hysteresis loop for low transverse fields. In both samples, the grains are tightly packed with little interstitial volume. (c). Schematic of magnetic grain coarsening with longitudinal field. As the longitudinal field increases, coarsening effects increase the average size of the magnetic domains, which can span several structural grains and can average out the intergrain disorder.

consistent with the tilting of a small fraction of the spins into the transverse plane. The small deviations from pure Ising behavior due to finite anisotropy demonstrate that the predominant effect of the transverse field is to create a site random field in the longitudinal direction. The evolution of the shape of the hysteresis loops as a function of H_T is more complex. The shoulder visible at low transverse field at $h_l \sim 3$ kOe in sample A along with the meeting of all of the curves at $h_l \sim 7$ kOe ($h_l \sim 10$ kOe for sample B) suggest that there are two regimes which should be considered separately; for $h_l < 7/10$ kOe, the loops narrow as the transverse field is increased, while above 7/10 kOe, the application of a transverse field actually broadens the hysteresis loops. Broadening, defined from the integrated area of the loops, cannot be explained by a simple coarsening of the domains or rotation of the spins as both effects act to decrease the stored energy of a ferromagnet and narrow the hysteresis loop. Instead, the broadening corresponds to an effective increase in the pinning potential beyond that already present in the zero-field random domain state, caused by the transverse field.

3.4 Return point memory

Due to the more clearly defined separation between the different field regimes and for the sake of clarity, we describe the behavior of sample A alone in fuller detail. We plot in Fig. 3.3(a) series of nested subloops for both $H_T = 0$ (Fig. 3.3(a),(c),(e)) and 6 kOe (Fig. 3.3(b),(d),(f)) in order to illuminate the underlying mechanisms in the different longitudinal field regimes, The subloops allow us to explore the energy hierarchies that form during nested longitudinal field trajectories. Each measurement starts at sufficiently high longitudinal field to saturate the magnetization along the applied field, followed by a ramp down to the starting field of the subloop sequence. The longitudinal field is then adiabatically ramped through a series of nested subloops (with the maximal hl decreasing by 1 kOe per subloop) that cover either the low or high longitudinal field ranges. As the subloop series progresses, the sample converges

on its equilibrium magnetization, and the series of nested loops corresponds to a hierarchy of energies at each "turning point" [39].

The subloops in the low longitudinal field regime (Fig. 3.3(d),(f)) narrow as the transverse field is applied, reflecting a decrease in the barriers to domain movement and consistent with the behavior of the full hysteresis loops shown in Fig. 3.3(c). Importantly, application of the transverse field does not change the essential self-similarity of the set of subloops. We contrast this evolution with the behavior of the nested subloops at high longitudinal field (Fig. 3.3(c),(e)). First, we note clear broadening in the presence of the transverse field. Second, we observe that the subloops at $H_T = 0$ exhibit the same sort of self-similarity exhibited in the low-field regime. With application of a transverse field, however, the self-similarity is lost and there is a monotonic change in slope of each subsequent nested subloop. Computer simulations [39] demonstrate that for small values of randomness below a critical threshold, hysteresis subloops maintain their self-similar nature and collapse onto the same full-scale hysteresis curve, but that in the strong randomness limit, subloops are no longer self-similar and scale inwards in a manner qualitatively similar to our experimental results at high longitudinal and transverse fields. This implies that the effect of the transverse field is to increase the relative strength of disorder and pinning.

The sharp steps in the magnetization that occur in the smallest low-field subloops for $H_T = 0$ (Fig. 3.3(e)) point to a small volume fraction of the sample exhibiting magnetically soft behavior with switching fields of order 1 kOe. This behavior can arise from a small number of grains of appropriate size and shape that are only weakly coupled to their neighbors, and thereby can easily rotate their magnetization to track the applied field. The disappearance of these low-field features upon application of a transverse field (Fig. 3.3(f)) is consistent with this interpretation, as the moments of these grains would simply rotate to point along the transverse direction and would not be detected in the longitudinal magnetization.

We pursue our interrogation of the relationship between transverse field, disorder, and

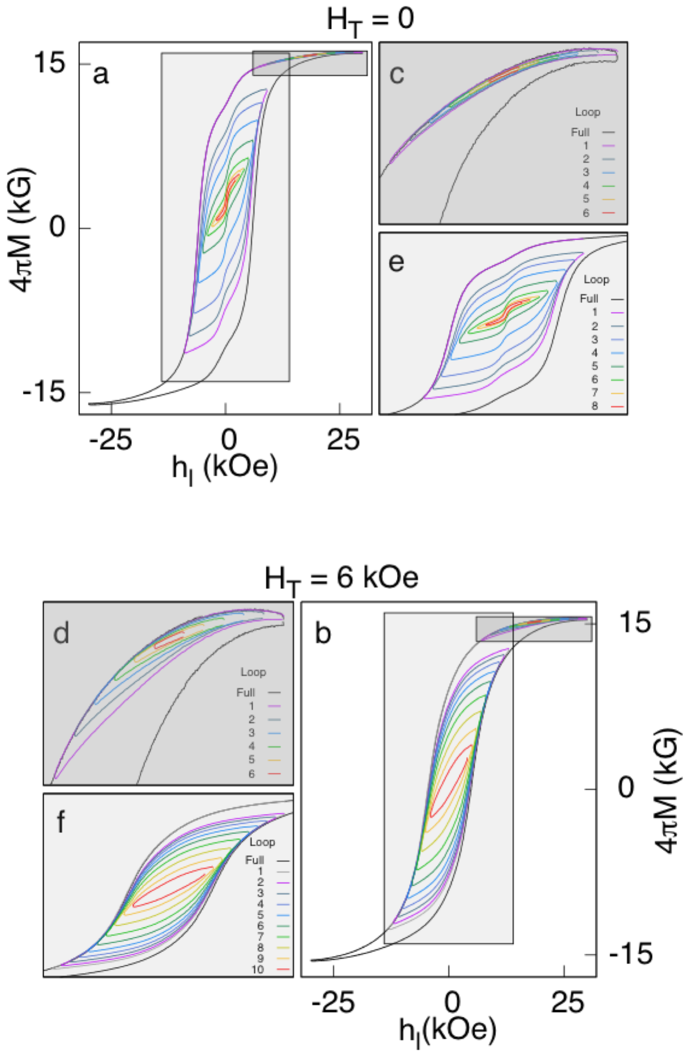

Figure 3.3: Effects of transverse field on subloop evolution (a),(b). Series of nested subloops (colored) inside overall hysteresis loops (black) at H_T=0 (a) and H_T=6 kOe (b),(c),(d). Nested subloops at high longitudinal field (centered on h_l= 18.5 kOe, with loop #1 ranging from 30 to 7 kOe, loop #2 ranging from 29 to 8 kOe, and following that sequence through the final loop which ranges from 20 to 17 kOe). In the absence of a transverse field (c). the subloop shapes remain self-similar. Applying a transverse field (d). broadens and rotates the subloops, destroying their self-similar nature. (e). Nested low longitudinal field subloops at $H_T = 0$, starting at loop #1 with $|h_l|$=9 kOe and decreasing for subsequent loops in maximum field by 1 kOe per loop, ending at #1 with $|h_l|$=3 kOe. (f). Nested low longitudinal field subloops at $H_T = 6$ kOe, starting at loop #1 with $|h_l|$=13 kOe and decreasing for subsequent loops in maximum field by 1 kOe per loop, ending at #1 with $|h_l|$=5 kOe. The subloops remain self-similar at zero (e). and 6 kOe (f) transverse fields.

domain dynamics through the method of return point memory (RPM) [40]. RPM is the ability of the material to arrive at the same microscopic configuration independent of the specific applied field path. Specifically, in a material possessing RPM, two independent applied field paths (not necessarily monotonic) with identical endpoints will arrive at the same microscopic configuration provided neither path exceeds the endpoint applied field values at any interior point of the trajectory [40–42]. RPM is solely a property of hard (as opposed to soft) magnets, and it provides a powerful probe of whether a given system is in a strongly disordered state such as a random-field-dominated regime [40].

We test return-point memory in Fig. 3.4 in the absence (a,b) and presence (c,d) of a transverse field. The field trajectory followed in the RPM measurements is sketched in the inset to Fig. 3.4(d). At constant H_T, the longitudinal field is cycled back and forth with the magnitude decreasing by 1 kOe per cycle, similar to the nested subloop measurements described above. The series of nested subloops forms a hierarchy of turning points at the end of each subloop. After the final cycle, h_l is smoothly ramped back up to the initial saturation value. In a material exhibiting RPM, whenever the return field matches the applied field of one of the turning points, the magnetizations will be equivalent (arrows in the inset), and the return path should intersect the hysteresis subloops at and only at each subloop endpoint [41]. Without the application of a transverse field, RPM breaks down above $h_l = 7$ kOe as the return curve falls below the original subloops (Fig. 3.4(b)). As h_l increases, characteristic domain sizes grow, spanning multiple grains, and the effects of the intrinsic disorder become proportionally weaker, leading to a loss of memory. Remarkably, a transverse field restores RPM. With $H_T = 6$ kOe, return point memory persists throughout the entire longitudinal field range (Fig. 3.4(c),(d)). The random fields induced by the transverse field at each grain boundary have increased the pinning potential to the point where the material remains in the strong-disorder limit up to magnetization saturation. In particular, the presence of return-point memory in this system demonstrates that the effects of the random fields dominate

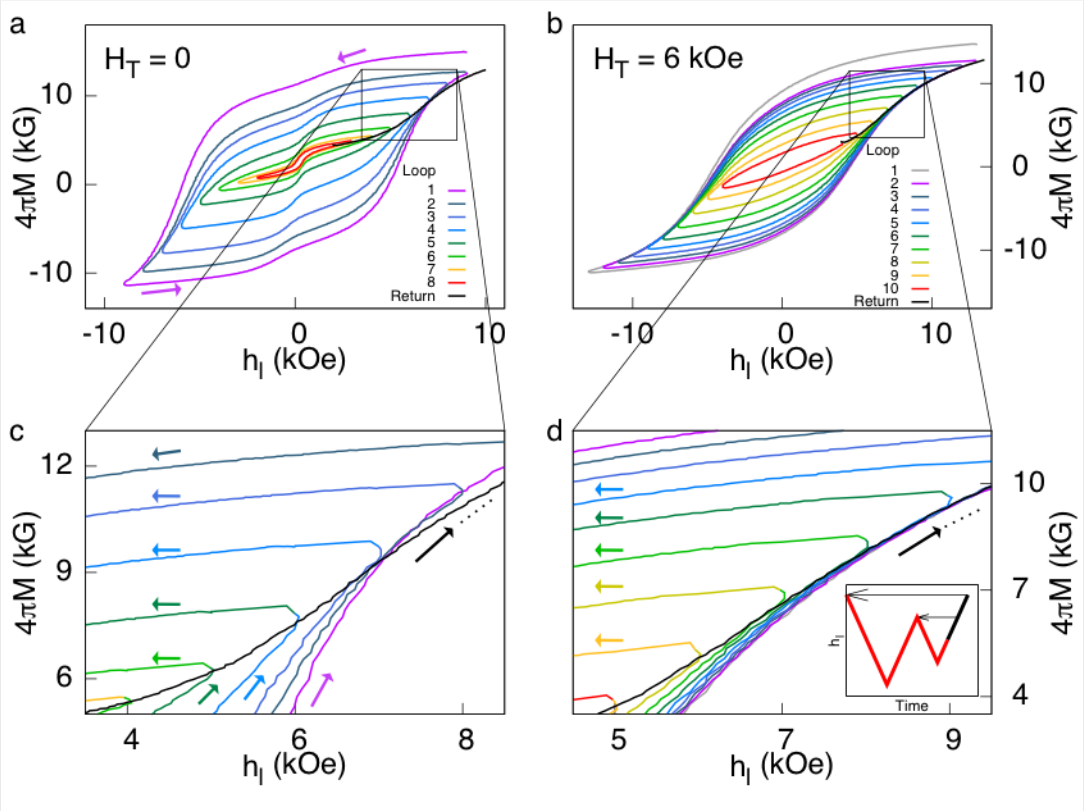

Figure 3.4: Transverse-field assisted return point memory. (a),(b). Return Point Memory in the absence of a transverse field. The longitudinal field is ramped in a decreasing triangle pattern, with $|h_l|$ starting at 9 kOe for loop #1 and decreasing by 1 kOe per subsequent subloop, followed by a linear ramp back up to saturation as sketched in the inset. Return-point memory, a characteristic signature of strong disorder, fails at $|h_l| = 7$ kOe, as seen by the crossing of the return line (black) through the original subloops (colored). (c),(d). Return point memory in transverse field of 6 kOe. The longitudinal field is ramped in a set of nested subloops starting with loop #1 at $|h_l|$=13 kOe and decreasing by 1 kOe steps per subloop to $|h_l|$=5 kOe, followed by a ramp back up to 30 kOe. Arrows show direction of field ramping along the subloop sequence and subsequent return to large longitudinal field. The return path does not cross the original set of subloops, demonstrating that applying a transverse field restores return point memory all the way to saturation by increasing the effective disorder through random-field effects. Insert: Schematic of return point memory. On the return path to saturation, the system retains memory of past magnetization extrema.

over the diagonal terms of the dipole-dipole interaction, as RPM is only manifest in the strong-disorder limit [40]. In light of the RPM results, we can return to the hysteresis loops presented in Fig. 3.2(c) and note that at low transverse field the randomness-dominated regime at low longitudinal field evolves into a weakly disordered regime at high field, with a plateau-like crossover region at $h_l \sim 7$ kOe. At high transverse fields, the enhancement of the random field effects means that the strong randomness regime persists to much larger longitudinal fields, eliminating the crossover region.

3.5 Conclusion

Experiments support the supposition that uniaxial grains in a common rare-earth ferromagnet behave as effective Ising dipoles, renormalizing the energy scale to room temperature and above. A transverse field can isothermally tune the pinning potential for magnetic domains from the weak disorder to the strong disorder limit. The off-diagonal terms in the dipole interaction, combined with the external field and the breaking of translational symmetry from the disorder, give rise to an effective random field [8, 9].

In the context of magnetic storage, this would allow entering a soft state for writing and switching to a hard reversal mode with a larger reversal energy for long-term retention and reading [43] Readily available, tunable random-field ferromagnets also would open up experimental studies of theoretical and computational predictions for the behavior of the RFIM. This would include the dynamics and distribution of avalanches during reversal, which should be accessible via Barkhausen noise techniques.

CHAPTER 4

BARKHAUSEN NOISE IN THE ROOM TEMPERATURE RANDOM FIELD ISING FERROMAGNET $Nd_2Fe_{14}B$

This Chapter is based on published material in "Barkhausen Noise in the Random Field Ising Magnet $Nd_2Fe_{14}B$", J. Xu, D.M. Silevitch, K.A. Dahmen, and T.F. Rosenbaum, Phys. Rev. B 92, 024424 (2015).

4.1 Introduction

With sintered needles aligned and a magnetic field applied transverse to its easy axis, the rare-earth ferromagnet $Nd_2Fe_{14}B$ becomes a room-temperature realization of the random field Ising model. The transverse field tunes the pinning potential of the magnetic domains in a continuous fashion. We plot in Fig. 4.1(a) and (b) the overall magnetic behavior of $Nd_2Fe_{14}B$ at T = 150 and 300 K, well below the $T_c = 585$ K Curie temperature [Herbst1984]. Increasing the temperature narrows the hysteresis loop for all field scales [Fig. 4.1(a)]. By contrast, applying a constant 6 kOe transverse field at T = 150 K results in several significant changes to the hysteresis loop [Fig. 4.1(b)]. First, there is a decrease of approximately 5% in the easy-axis component of the saturation magnetization, due to the finite value of the intrinsic anisotropy and consequent tilting of spins away from the Ising (easy) axis. Second, the shape of the loop changes when the transverse field is applied. As discussed in detail in Chapter 3 and Ref. [13], a transverse field decreases the enclosed area of the hysteresis loop for longitudinal fields below 15 kOe, while for larger longitudinal fields, applying a transverse field increases the loop area. This broadening is a signature of enhanced pinning in the high-field regime where the typical domain size is large due to coarsening, also substantiated by studies of return-point memory trajectories [13, 44].

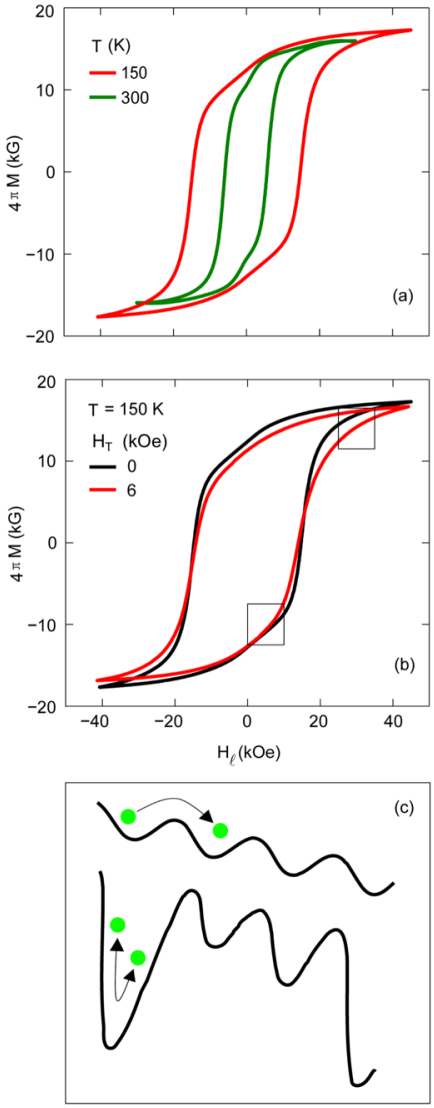

Figure 4.1: Overview of the magnetic hysteresis in $Nd_2Fe_{14}B$. (a) Hysteresis loops at T = 150 and 300 K. Thermal fluctuations monotonically narrow the hysteresis loop at elevated temperature. (b) Hysteresis loops at T = 150 K, with magnetization measured parallel to the Ising (easy) axis in static 0 and 6 kOe transverse magnetic fields. Application of a transverse field changes the shape of the loop, narrowing it at low longitudinal field and broadening it at high longitudinal field. The latter is an indication of enhanced pinning. Boxes at low and high longitudinal field show the ranges for the Barkhausen data plotted in Fig. 4.2 and 4.3, respectively. (c) Schematic showing the evolution of the free-energy landscape when a transverse field is applied. The transverse-field-induced random field tunes the system from the weak to the strong disorder limit, resulting in deeper local minima in the energy landscape, where the magnetization can oscillate about these minima.

4.2 Barkhausen noise in $Nd_2Fe_{14}B$

In order to study the domain reversal dynamics in the weak and strong pinning regimes, we performed Barkhausen measurements across full hysteresis loops for requisite transverse fields and temperatures. A schematic of the energy landscape is shown in Fig. 4.1(c), where the combination of intrinsic and extrinsic pinning with the constantly ramping longitudinal field produces a tilted washboard potential for the magnetization state of the system. In the weak-pinning limit (top row), the relatively shallow minima allow the system to progress monotonically through the set of minima, resulting in a series of single-signed pulses in $\frac{dM}{dt}$ and hence single-signed spikes in the induced voltage. This is the behavior typically observed in Barkhausen experiments on magnetically soft and amorphous materials such as ferroglasses [32, 45–48]. By contrast, increasing the depth of a number of the pinning wells (bottom row) can result in qualitatively different behavior. It becomes possible for a large reversing domain to overshoot its ultimate equilibrium point and oscillate about the center of the potential well. This results in transitory oscillatory behavior in the magnetization as the system comes to equilibrium, and hence oscillatory behavior in the pickup coil voltage. Behavior of this kind was recently reported [31] in a steel alloy in which uniaxial stress was used to enhance the strength of the pinning.

The salient features of our experiments are captured in Fig. 4.2 and 4.3. These plots present raw time series of the voltage induced in a pickup coil surrounding a $Nd_2Fe_{14}B$ cylinder for two segments of the hysteresis loop at T = 150 K [Fig. 4.1(b)] in three fixed transverse fields. At the low longitudinal fields of Fig. 4.2, the system consists of an ensemble of small domains that reverse monotonically as the longitudinal field is ramped, following the behavior sketched in the top row of Fig. 4.1(c). The rate of occurrence of visible Barkhausen spikes drops as the strength of the disorder increases with increasing transverse field. This suggests that enhancing the disorder-induced pinning in this regime suppresses avalanches consisting of multiple domains reversing in quick succession to produce an observable voltage

spike and forces the system towards a magnetization change dominated by small domains reversing individually, causing voltage spikes which are at or below the noise floor of our measurement chain [49].

As shown in the successive enlargements of Fig. 4.2(b) and (c), the observable events typically last less than 10 μs in duration. The fast dynamics are a result of the strong pinning in general in $Nd_2Fe_{14}B$; in the ferroglasses and other soft materials more commonly investigated using Barkhausen techniques, the reversal time scales are typically two to three orders of magnitude longer [32, 47, 48]. These events, while fast compared to other disordered magnets studied using Barkhausen techniques, are still substantially slower than the GHz-scale speed of the intrinsic reversal rate of an individual microscopic domain of $Nd_2Fe_{14}B$ [50]. The observed events consist of collective modes or cascades rather than single domain reversals. Within the accessible range of our superconducting magnet, no variation in the histograms was seen as a function of longitudinal field ramp rate (see Chapter 2), indicating that the measurements were taken in the adiabatic limit [51].

At the high longitudinal fields of Fig. 4.3, we observe different signatures in the Barkhausen noise spectra. Domain coarsening effects result in large domains so that even the reversal of an individual domain can produce a detectable signal. As the strength of the pinning is again increased by ramping the transverse field, we now see an increasing frequency of events where the magnetization oscillates repeatedly, corresponding to the physical picture at the bottom of Fig. 4.1(c). The typical oscillation period is of the order of a few tens of microseconds, with the ringdown period of the entire event lasting for a few tens of milliseconds [Fig. 4.3(b) and (c)], indicating a relatively low degree of anharmonicity in the local pinning potential. We note that even in the low temperature limit the application of a transverse field is still required to induce magnetization oscillations.

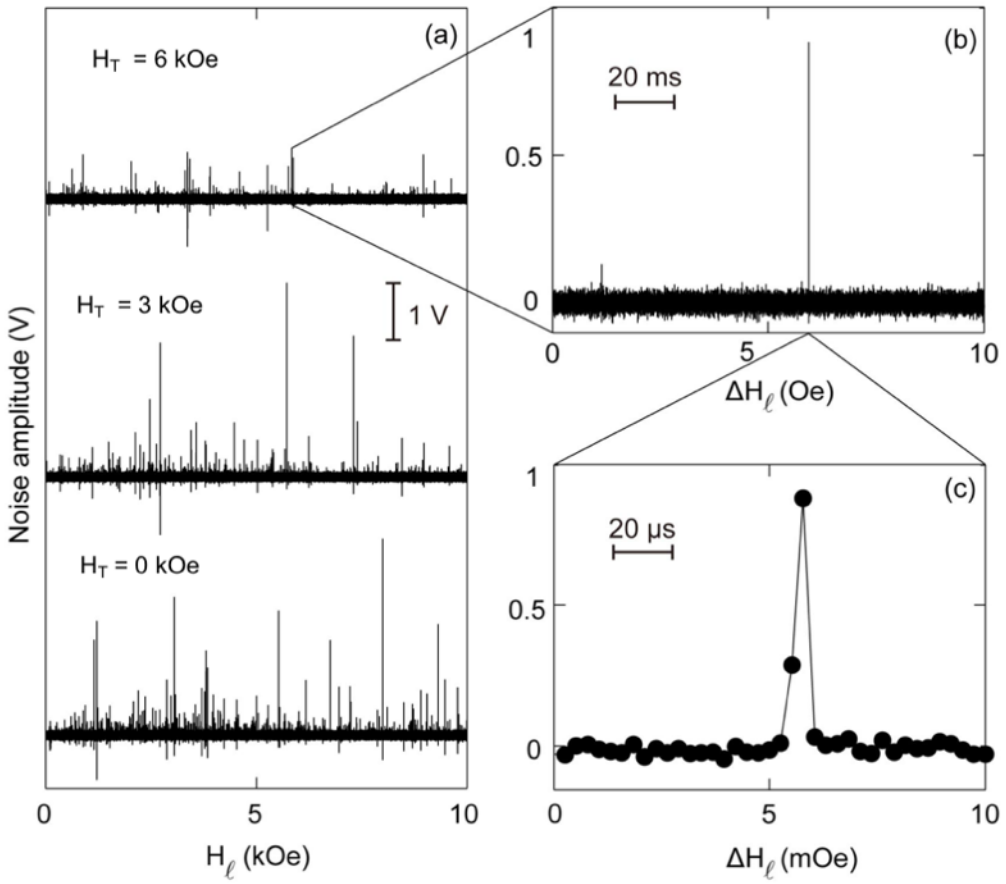

Figure 4.2: Time series of induced voltage on a pickup coil wrapped around a $Nd_2Fe_{14}B$ cylinder at T = 150 K, low longitudinal field (increasing continuously at 0.4 T/min), and a series of transverse fields. (a) At low longitudinal fields, the absence of domain coarsening gives time series dominated by single-signed pulses, corresponding to monotonic changes in the magnetization. (b),(c) Successive enlargements of one reversal event at 6 kOe transverse field, showing the pulse structure over a duration of approximately 8 μs.

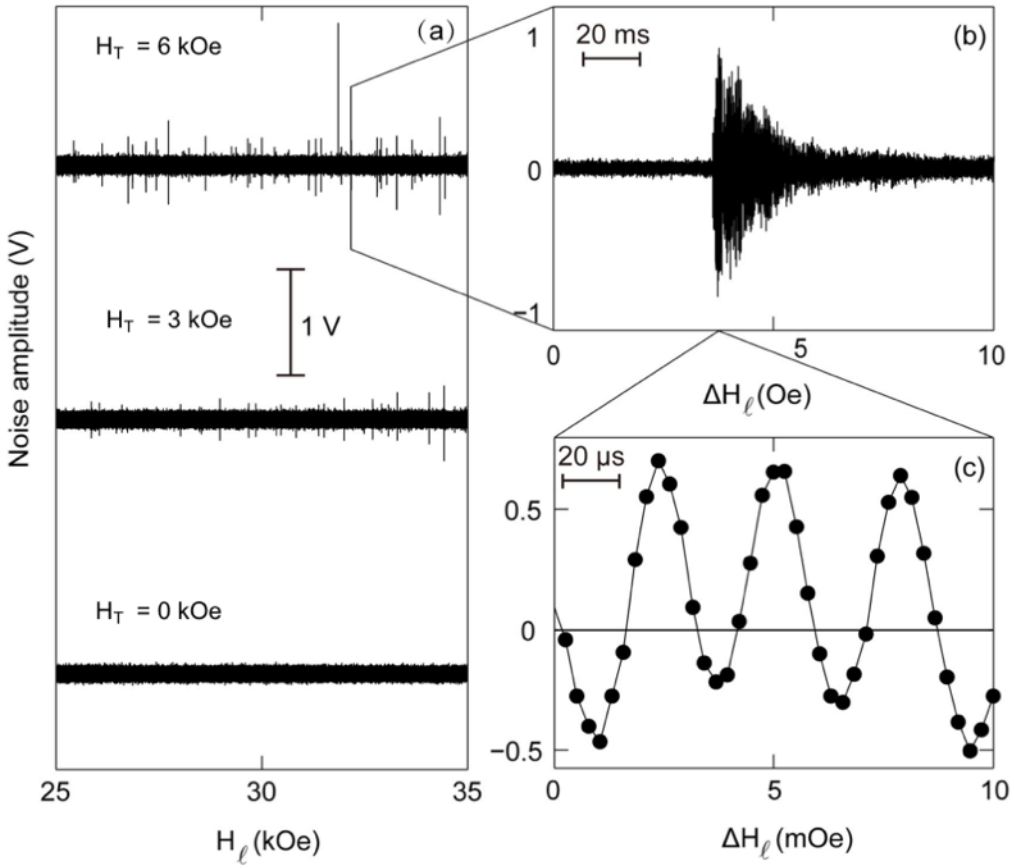

Figure 4.3: Time series of induced voltage on a pickup coil wrapped around a $Nd_2Fe_{14}B$ cylinder at T = 150 K, large longitudinal field (increasing continuously at 0.4 T/min), and a series of transverse fields. In contrast to the behavior at low longitudinal fields (cf. Fig. 4.2), the deep potential energy wells created by the combination of domain coarsening and the random-field-induced pinning enable magnetization oscillations. (a) Time series for a range of transverse fields. In the absence of a transverse field, the system is in the weak disorder limit and evolves in a nearly continuous fashion. As the transverse field is increased, the strength of the disorder increases, giving a steadily increasing number of discrete events. (b),(c) Successive enlargements of a single event at a longitudinal field of 3.2 T. The overall duration of the oscillatory event is approximately 30 ms, with an oscillation period of 44−48 μs (11−12 sampling points).

4.3 Probability distributions, power laws, and their breakdown

The dynamics of the monotonic switching events of the type plotted in Fig. 4.2 can be investigated by examining probability distribution histograms of different moments of the events and studying the evolution of the distributions as a function of temperature and transverse field. These probability distributions are shown in Fig. 4.4 for the integrated area $S = \int (V - V_0)dt$ (Fig. 4.4(a)) and the total event energy $E = \int (V - V_0)^2 dt$ (Fig. 4.4(b)), where V is the amplified time-dependent voltage and V_0 is the measured noise floor of the amplifier chain. S is proportional to the total change in magnetization associated with a given reversal event, whereas E measures the energy dissipated over the course of the event [17].

We observe power-law behavior for both S and E. As a function of temperature and transverse field, the critical exponents fall into two groups. At T = 4.2 K and H_T = 3 and 6 kOe, and at T = 150 K and H_T = 6 kOe, the exponents are 2.3 ± 0.2 and 1.9 ± 0.2 for the distributions of S and E, respectively. The exponents for S and E are comparable to the values 9/4 and 11/6 predicted from mean-field theory [49, 52], as would be expected for a long-range interaction such as dipole-dipole coupling. Moreover, the energy distribution demonstrates a power-law relationship to the area (Fig. 4.4(b) inset) with exponent 1.64 ± 0.1, not far from the value of 1.5 predicted from mean-field theory [49]. For all transverse fields at T = 300 K, as well as the low field behavior at lower temperatures, we find a different set of critical exponents: 3.5 ± 0.4 for S and 2.4 ± 0.3 for E. This bimodal behavior suggests that we can divide the system into two regimes, the first where the disorder induced by the transverse field dominates over thermal effects and the second where the thermal behavior dominates. In the disorder-dominated regime, we see behavior broadly consistent with the mean-field expectation.

Importantly, the power-law behavior does not extend to the limits of the probability distribution. As can be seen from the dashed lines in Fig. 4.5, which are extrapolations of

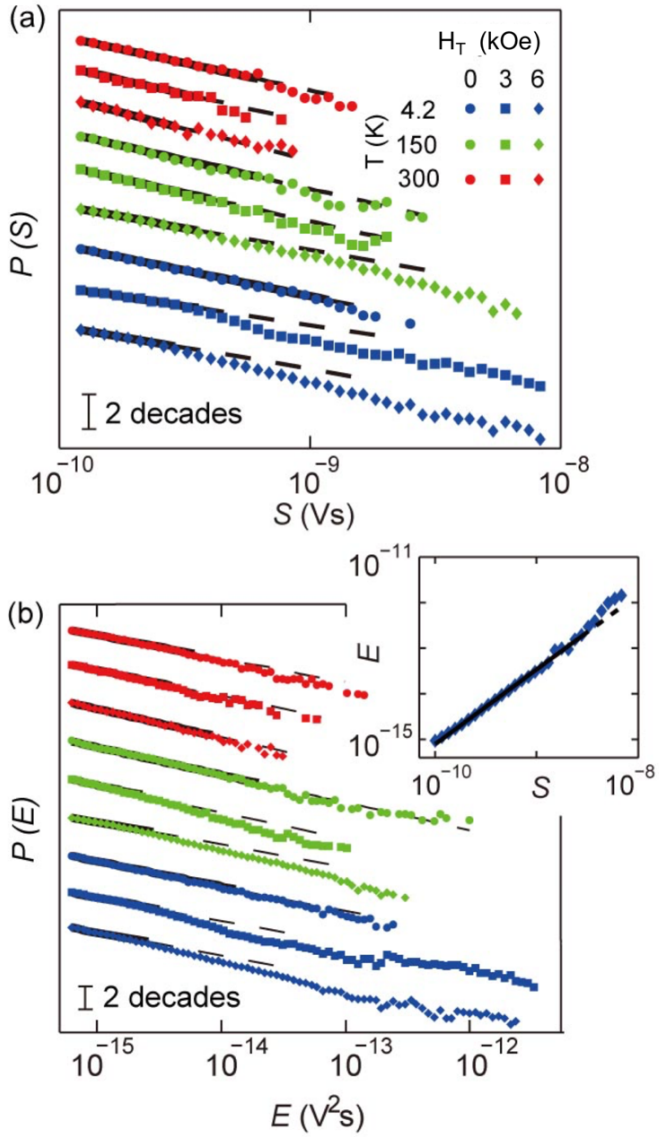

Figure 4.4: Probability distributions of avalanche energies and sizes for T = 4.2, 150, and 300 K, and transverse fields H_T = 0, 3, and 6 kOe, in the low longitudinal field regime plotted in Fig. 4.2. Solid lines are fits showing the extent of pure power-law behavior; dashed lines are extrapolations of those fits, showing deviations from the power laws. Traces are offset vertically for clarity. (a) Probability distribution of integrated event area S. The exponents top to bottom are 3.1(0.4), 2.2(0.2), 2.5(0.3), 3.5(0.4), 3.6(0.5), 2.5(0.3), 3.5(0.4), 3.7(0.8), and 3.3(0.6). (b) Probability distribution of event energies E. The exponents top to bottom are 2.2(0.3), 2.0(0.2), 1.9(0.2), 2.3(0.2), 2.8(0.4), 1.9(0.2), 2.4(0.2), 2.3(0.7), and 2.5(0.5). Inset: avalanche size versus energy at H_T = 6 kOe and T = 4.2 K. Solid line is a power-law fit with exponent 1.64 ± 0.1.

the power-law fits, the measured histograms fall off from the power law at large S and E. This cutoff in the size and energy distributions of avalanches is a signature of a disorder-dominated system [49, 52]. For the RFIM in particular, the cutoff is expected to follow $S_{max} \sim (R - R_c)^2$, where S_{max} is the size of the largest avalanche for which power-law behavior is expected, R is a measure of the strength of the disorder, R_c is a critical level of disorder, and the exponent σ is $\frac{1}{2}$ in the mean-field limit [52].

We plot in Fig. 4.5 the measured deviations from power-law behavior in the energy spectrum of the avalanches at T = 300 K for a series of transverse fields. Given that we are testing the effects of disorder, we include in this analysis avalanches from both low (Fig. 4.2) and high (Fig. 4.3) longitudinal fields; qualitatively similar conclusions can be drawn from considering only the single-signed Barkhausen signatures of Fig. 4.2 and 4.4. In the absence of a transverse field, the disorder effects in $Nd_2Fe_{14}B$ are relatively weak, and the power-law behavior extends out to the highest avalanche energies. When a transverse field is applied, the strengthening of the pinning associated with the effective random field yields a larger effective disorder, resulting in a cutoff from the power-law at systematically lower avalanche energies. This experimental result dovetails nicely with the predictions from the numerical simulations of the effects of increasing disorder [52–54].

Finally, we consider separately the magnetization reversal events prevalent at large longitudinal fields. Instead of a monotonic reversal of a domain or series of domains resulting in a single-signed peak in the induced voltage, in this regime we see events consisting of a well-defined sinusoidal oscillation which rings down over the course of 1000 or more periods (Fig. 4.3). As the induced voltage is proportional to $\frac{dM}{dt}$, this is indicative of an oscillation in the magnetization itself. Such an oscillation requires a well-defined harmonic minimum in the free energy landscape, along with a significant degree of overshoot on the initial transition into that minimum. The first requirement suggests that the prevalence of such oscillatory events will be enhanced with increasing transverse field and hence the increasing strength

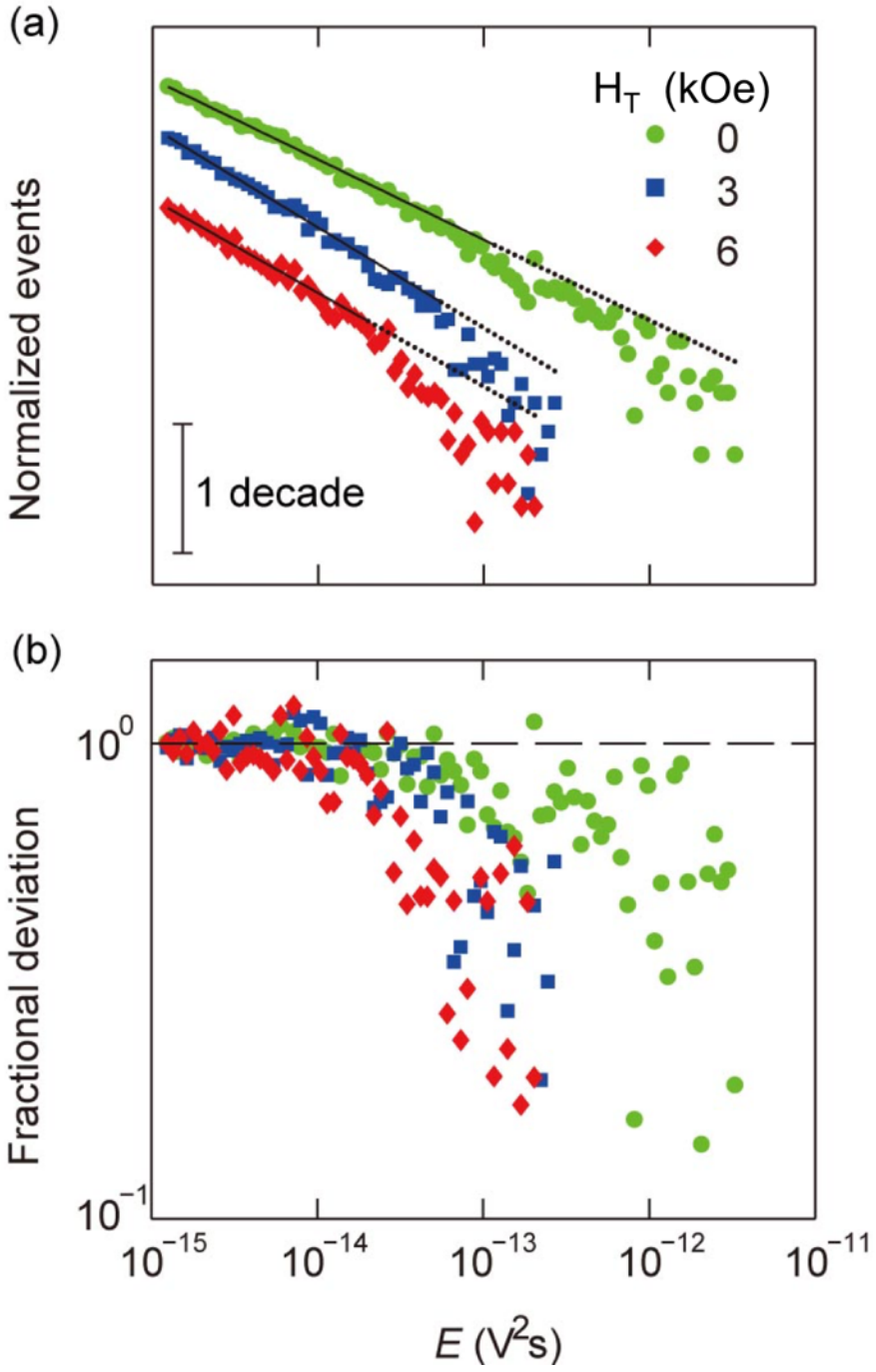

Figure 4.5: Departures from power-law behavior in the avalanche energy distribution. (a) T = 300 K avalanche energy distribution for a series of transverse fields fitted to a power law; traces are offset vertically for clarity. (b) Fractional deviation from power-law behavior, showing measured probability distribution divided by the individual fitted power laws. Transverse-field-induced randomness causes systematically more profound deviations from the power-law form.

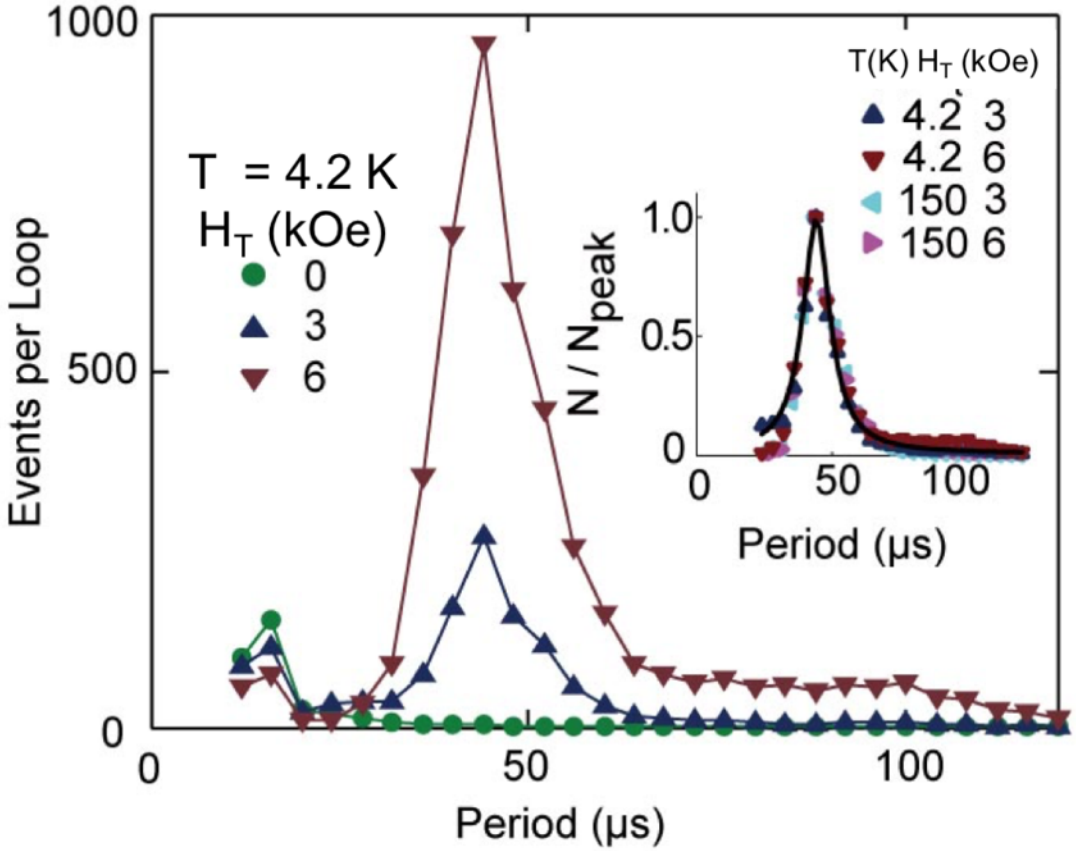

Figure 4.6: Distribution of periods for oscillatory magnetization events at T = 4.2 K and a range of transverse fields. Increasing the transverse field increases the rate of occurrence of the oscillation events, while the characteristic oscillation period remains constant. Inset: normalized distribution of oscillation periods for T = 4.2 and 150 K and H_T = 3 and 6 kOe, demonstrating that the shape of the distribution is essentially independent of both temperature and transverse field. Smooth curve is a Lorentzian fit simultaneous to all four temperature/field sets.

of random-field-induced pinning. The large amount of inertia associated with the second requirement limits this effect to large domains reversing as a single unit, i.e. primarily in the large longitudinal field regime where coarsening has increased the typical domain size.

In order to assess whether there is a single energy scale associated with these oscillatory events, we show in Fig. 4.6 probability distributions for the oscillation period for T = 4.2 K and a series of transverse fields. There are two characteristic periods for the oscillation events, with a small number of events exhibiting a 16 μs (4 pixel) period and the majority of the events showing periods ranging from 30 to above 100 μs, with the predominant period at 44 μs. With the application of a transverse field and stronger pinning, there is marked increase in the occurrence rate. This occurrence rate is the primary avenue for temperature and transverse-field dependence (Fig. 4.6 inset). The peak period and shape of the distribution curve are largely independent of the external variables, suggesting that the ratio of typical domain size in the coarsening limit to the depth of the pinning well is essentially constant and both quantities scale similarly as the disorder strength is tuned upwards via the transverse field.

A small number of short-period oscillation events are also observed at low longitudinal fields. Unlike the longer-period events in the high-longitudinal field regime, these overshoots have a typical lifespan of approximately 2 periods, presumably due to small domains oscillating in much softer harmonic wells. When a transverse field is applied and the strength of the pinning wells is increased, these short oscillation modes are progressively suppressed and monotonic reversal events dominate the probability distribution.

4.4 Scaling laws and critical exponents

We compare our measurements with the results of numerical simulations of the RFIM by examining a scaling collapse of the probability distributions of the event sizes for different temperatures and transverse fields. Following the approach of Ref [54], we attempt to scale

the probability distributions using the functional form $D(rS^{\sigma}) = \lim_{R \to R_c} S^{\tau+\sigma\beta\delta} D(S,R)$, where $\tau + \sigma\beta\delta$ is the exponent describing the cutoff threshold, $\tau + \sigma\beta\delta$ parameterizes the slope of the probability distribution integrated around a complete hysteresis loop above the cutoff, and $r = \frac{R-R_c}{R}$ is a reduced disorder [54]. We plot in Fig. 4.7(a) χ^2 contours for the scaling of all nine temperature/transverse field values as a function of the two scaling exponents. We see that the best-fit value for the cutoff threshold exponent σ is 2/3 for all fits, with only a weak dependence on temperature and transverse field. This value exceeds the mean-field prediction of 1/2, but lies closer to it than the value of 1/4 calculated for nearest-neighbor interactions in d=3 [52]. By contrast, we find that the best-fit values for $\tau + \sigma\beta\delta$ fall into two classes depending on temperature and transverse field.

In the disorder-dominated regime (transverse field large compared to temperature), the probability distributions can be scaled on top of each other with little scatter (Fig. 4.7(b) and (c)). In this regime, at T = 4.2 K and H_T = 3 and 6 kOe, as well as T = 150 K and H_T = 6 kOe, the area probability distributions have best-fit values of $\tau + \sigma\beta\delta = 2.6 \pm 0.25$, where as reported above $\sigma = 0.67 \pm 0.02$. This value of $\tau + \sigma\beta\delta$ compares to the mean-field expectation of 2.25 and the nearest-neighbor value of 2.03 [52]. A similar scaling collapse analysis on the energy distribution for the same set of temperatures and transverse fields yields $\sigma_E = 0.33 \pm 0.04$ and $(\tau+\sigma\beta\delta)_E = 2.1 \pm 0.2$, compared to mean-field predictions of 1/3 and 11/6 respectively [49]. The probability distributions for this disorder-dominated regime can be scaled on top of each other with little scatter (Fig. 4.7(b) and (c)). By contrast, for all transverse fields at T = 300 K, along with 0 and 3 kOe at T = 150 K and 0 kOe at T = 4.2 K, $\tau + \sigma\beta\delta = 3.7 \pm 0.4$. In this thermally-dominated limit, the observed best-fit exponents are well away from the predictions for both mean-field and nearest-neighbor interactions. The scaling is of marginal quality as shown in Fig. 4.8, suggesting that this regime is best understood as a qualitatively different regime from the randomness-dominated regime and that a strong-disorder model is not appropriate.

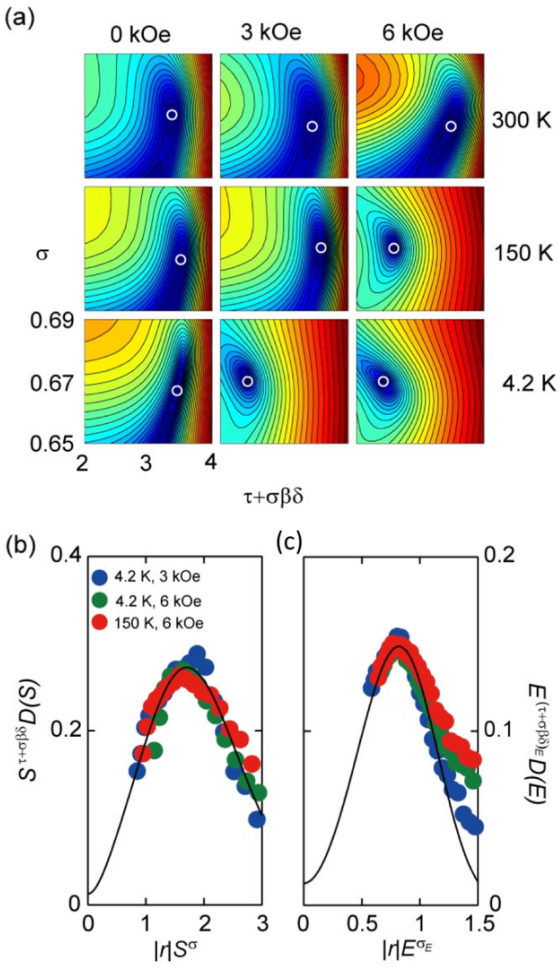

Figure 4.7: Scaling behavior in the strong disorder limit. (a) χ^2 contours for the avalanche area scaling parameters σ and $\tau + \sigma\beta\delta$. White circles mark the locations of the best-fit minima, with deviations ranging from small (blue) to large (red). Two distinct classes of behavior are observed. At large H_T and small T, where domain pinning is strong, there is a narrow minimum at $\sigma = 0.67 \pm 0.02$ and $\tau + \sigma\beta\delta = 2.6 \pm 0.25$. At smaller fields and/or larger temperatures, where pinning cannot compete with thermal fluctuations, qualitatively different scaling behavior is observed. There is a well-defined minimum at and a broader dependence on with the absolute minimum remaining at 0.67±0.04. (b), (c) Scaling collapses for the size and energy distributions in the strong disorder limit (T = 4.2 K, H_T = 3 and 6 kOe, and T = 150 K, H_T = 6 kOe). The solid lines are a phenomenological function from Ref. [54]. The scaling parameters for the size distribution (b) were $\sigma = 0.67$ and $\tau + \sigma\beta\delta = 2.53, 2.47, 2.70$ from top to bottom and for the energy (c) were $\sigma_E = 0.67$ and $(\tau + \sigma\beta\delta)_E = 2.2, 2.2, 2.1$.

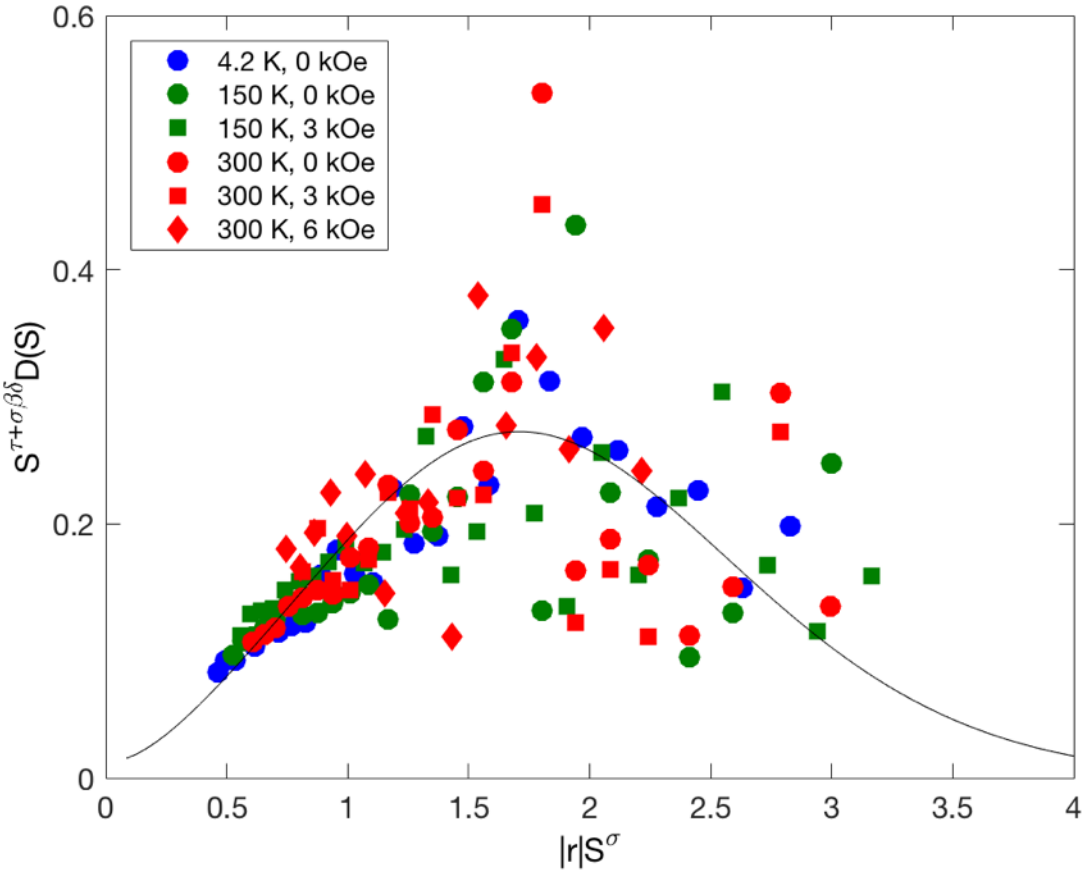

Figure 4.8: Scaling collapse in the thermally-dominated regime for all transverse fields at T = 300 K, along with 0 and 3 kOe at T = 150 K and 0 kOe at T = 4.2 K. Compared with Fig. 4.7(b) the scaling collapse is of marginal quality.

4.5 Conclusion

While the avalanche dynamics of the Random Field Ising Model have been studied extensively via theoretical modeling and numerical simulations, the difficulty of realizing the RFIM in bulk ferromagnets has limited the experimental possibilities. The aim of this work has been to begin to fill that gap. We have studied the reversal dynamics of the sintered rare-earth ferromagnet $Nd_2Fe_{14}B$ in a transverse field, a room-temperature realization of the Random Field Ising Model. The power-law exponents and scaling forms of Barkhausen noise events as a function of temperature and transverse field demonstrate that the system can be placed into two disjoint regimes depending on tunable disorder: a strong-randomness regime in which the random-field-induced pinning dominates and a thermal regime in which fluctuations dominate. In the strong randomness regime, the critical exponents are close to mean-field predictions for heavily disordered systems. Moreover, the deep free-energy minima allow for domain-wall oscillations for extended periods of time. Having demonstrated the feasibility of using Barkhausen techniques to access the domain dynamics in this bulk random-field magnet, it should be possible to extend this technique to single-spin, dipole-coupled, random-field magnets like $LiHo_xY_{1-x}F_4$ and Mn_{12-ac}, where the random-field dynamics are enriched by the addition of quantum tunneling terms to the Hamiltonian. We discuss this extension in Chapter 5.

CHAPTER 5

BARKHAUSEN NOISE IN THE ISING FERROMAGNET $LiHo_{0.65}Y_{0.35}F_4$

5.1 Phase diagram

The magnetic phases of dipolar-coupled $LiHo_xY_{1-x}F_4$ have been studied as a function of dipole concentration x, temperature T and transverse field H_T. In the x-T phase diagram, the material is a full-moment ferromagnet for x $>$ 0.46 [55]. The Curie temperature is suppressed as T_c(x) = xTc(x=1), following mean-field scaling [11, 55]. With higher doping concentration, the disorder and frustration arising from the anisotropic dipole-dipole interaction give rise to a spin-glass ground state [55]. The whole x-T phase has been mapped out using neutron diffraction, magnetic susceptibility and specific-heat measurements through a series of studies [55–58]. Here we focus on the high concentration x=0.65 where the ground state is unambiguously ferromagnetic.

The T-H_T phase plane for pure $LiHoF_4$ was first determined from susceptibility measurements earlier in our group [26]. It displays a critical field of Hc = 49.5 kOe at zero temperature and T_c =1.53 K at zero transverse field, as indicated in Fig. 5.2. The quantum critical behavior is mean-field-like as is theoretically shown that the ground state of d-dimensional transverse field Ising model is equivalent to (d+1)−dimensional Ising model at finite temperatures [59, 60]. The experimental results such as magnetic susceptibility measurements match very well with mean-field theory both in classical and quantum limit [26]. For example, by fitting $\chi' \propto h^{-\gamma}$, where χ' is the susceptibility and reduced transverse field $h = |H_T - H_T^c|/H_T^c$ and H_T^c is the critical transverse field at zero temperature, within error bars $\gamma = 1$ for temperatures down to 50 mK [26]. Furthermore, by solving the effective Hamiltonian by replacing the spin-spin interaction with an averaged coupling constant, it has been shown that the entire phase diagram can be quantitatively explained by mean-field

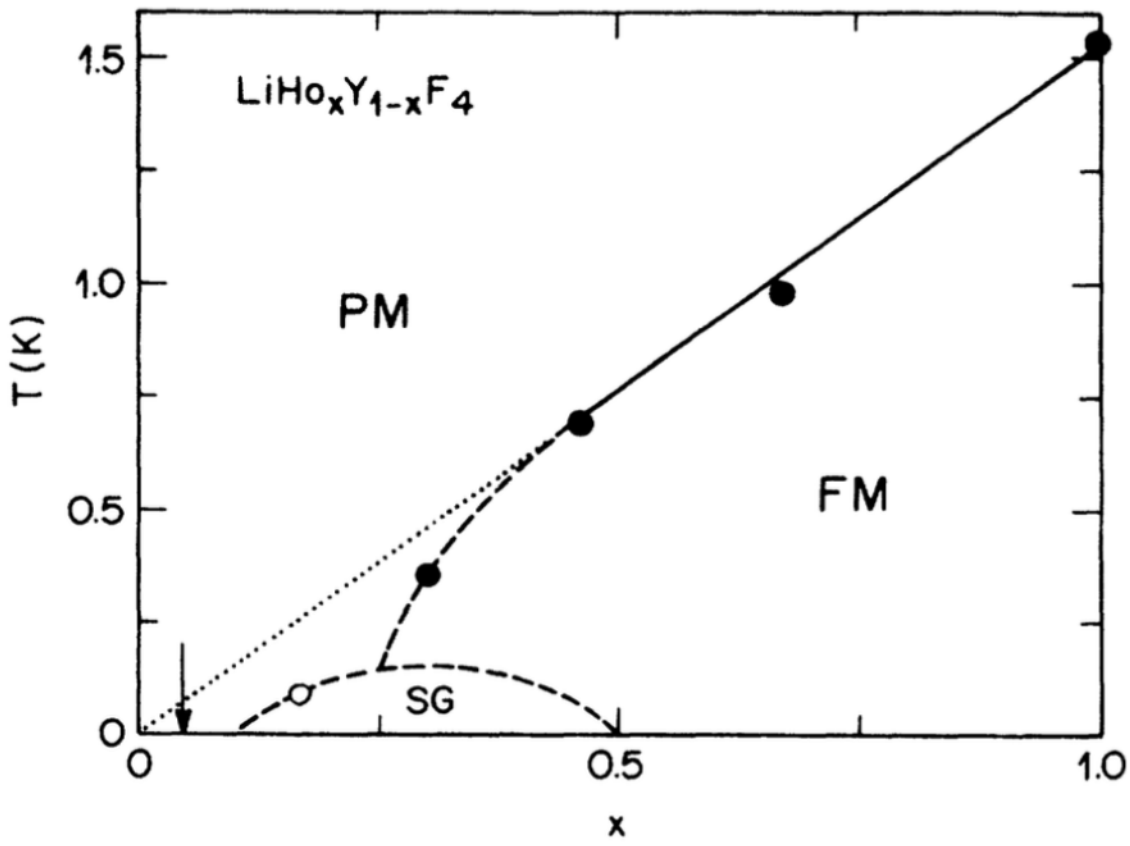

Figure 5.1: Phase diagram for the diluted dipolar-coupled Ising magnet, $LiHo_xY_{1-x}F_4$. PM = Paramagnet, FM = Ferromagnet, SG = Spin Glass. Solid circles are from neutron and magnetic susceptibility measurements [55–57]. The open circle denotes a spin-glass transition temperature obtained from a dynamic scaling analysis of the x =0.167 susceptibility data. From Ref. [55].

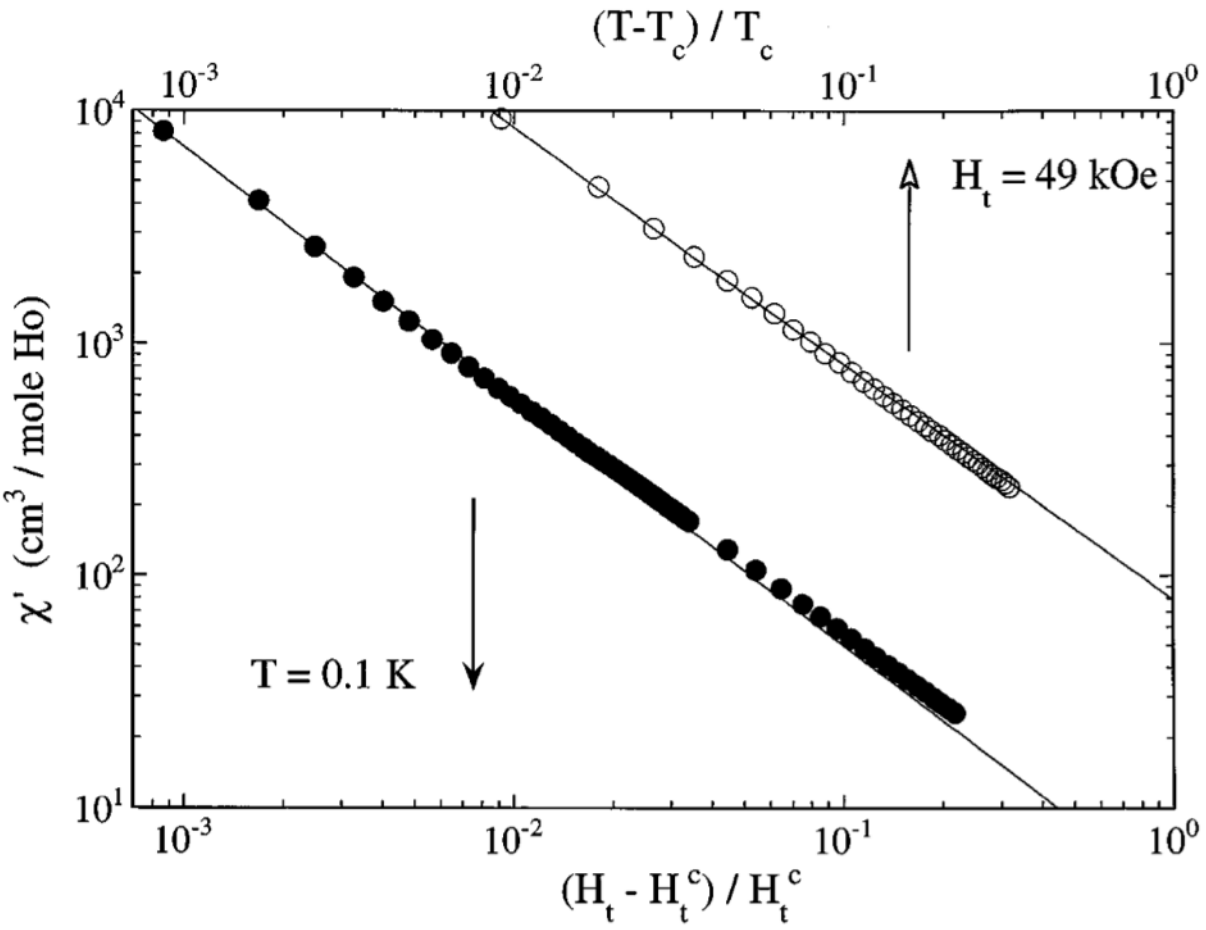

Figure 5.2: Log-log plot of susceptibility vs reduced transverse field. The exponent shows remarkable agreement with mean-field critical behavior. Open circles show χ' vs reduced temperature and filled circles show χ' vs reduced transverse field. From Ref. [26].

theory, including the hyperfine interaction.

When the system is doped, the critical transverse field H_T is suppressed at zero temperature and the Curie temperature at zero transverse field scales as $T_c(\mathrm{x}) = \mathrm{xTc(x{=}1)}$. Experimentally, the Curie temperatures for x = 1, 0.65 and 0.44 are 1.53, 1.02 and 0.669 K, respectively. Fig. 5.3 shows the normalized phase diagram for disordered materials where the normalized factors are the quantum tunneling strength and the Curie temperature in the pure sample. The x=1 curve is the mean-field calculation considering a Hamiltonian that includes the hyperfine interaction and the dipole-dipole interaction. The critical temperature is suppressed for higher doping because higher disorder amplifies the effective random field

at each site, thereby introducing stronger spin mixing between the two originally degenerate ground states. The long-range ordering becomes more easily destroyed with stronger quantum fluctuations as a transverse field is applied perpendicular to the Ising axis. There is also a clear discrepancy in the phase boundary between experiments on diluted crystals and mean-field theory, as indicated in the Fig. 5.3 inset. The critical behavior $\chi^{'} = \Gamma^{\frac{1}{\delta}-1}$ near T_c for the diluted system finds a critical exponent $\frac{1}{\delta} - 1 = -0.57 \pm 0.03$ [11], which is different from the value of -1 mentioned above in the mean-field prediction [11].

5.2 From classical spin pinning to quantum speedup

Following the discussion in Chapter 1, let's start with the effective Hamiltonian in a diluted system with an effective random field h_i:

$$H_{eff} = -\sum_{ij} J_{ij}\sigma_i^z\sigma_j^z - \sum_i h_i\sigma_i^z - \Gamma\sum_i \sigma_i^x \tag{5.1}$$

where J_{ij} is the general pairwise spin interaction, implicitly a function of transverse magnetic field, and Γ denotes the transverse magnetic field with its accompanying quantum fluctuations [1]. $\Gamma = \Delta(B_x)$ where $\Delta(B_x)$ is the energy gap between the two originally degenerate ground states. Hence Γ sets the quantum tunneling rate [1]. while the second term in the Hamiltonian sets the effective domain pinning strength. In a classical ferromagnet where domain nucleate at local pinning centers, the driving force to flip a magnetic domain is the local field, which, in our case, combines the applied longitudinal field and the effective random field h_i. Increasing the random field h_i will increase the energy barriers for domain reversal and broaden the hysteresis loop [13, 61]. In a quantum magnet, however, the effects of applying a transverse field are more complicated. It not only creates the effective random h_i but also introduces the quantum tunneling effect Γ. Both terms originate from quantum fluctuations, but have different physics effects. Fig. 5.4 shows the domain reversal for the two

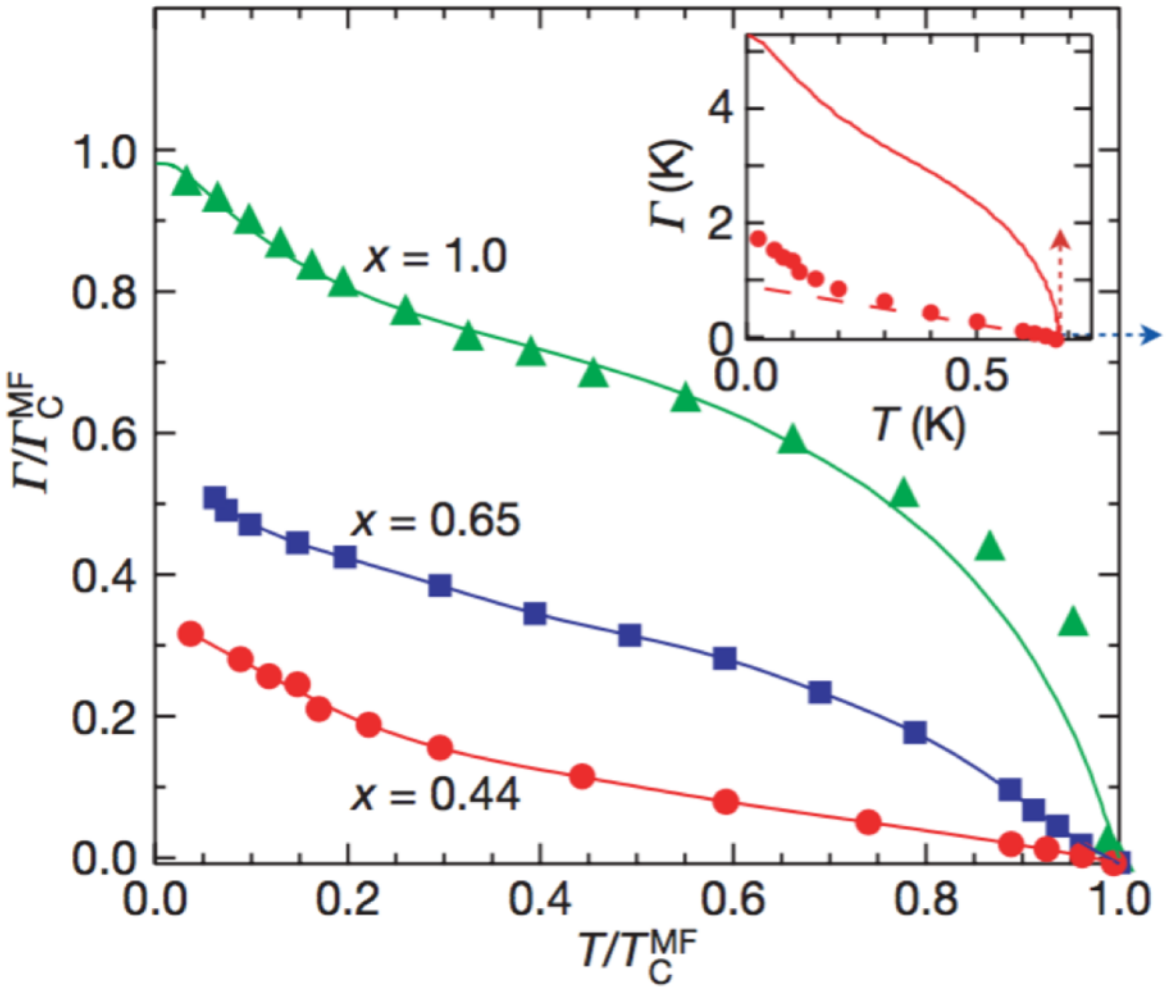

Figure 5.3: Normalized phase diagram for $LiHo_xY_{1-x}F_4$. The normalization factor Γ_C^{MF} and T_C^{MF} are mean-field prediction of quantum tunneling strength and Curie temperature for the pure sample. Inset: the red dots are the phase boundary for the x= 0.44 sample in absolute units. The red solid line is the mean-field prediction using parameters for the pure sample. The red dashed line is the phase boundary calculated from critical divergences observed in magnetic susceptibility measurements. From Ref. [11].

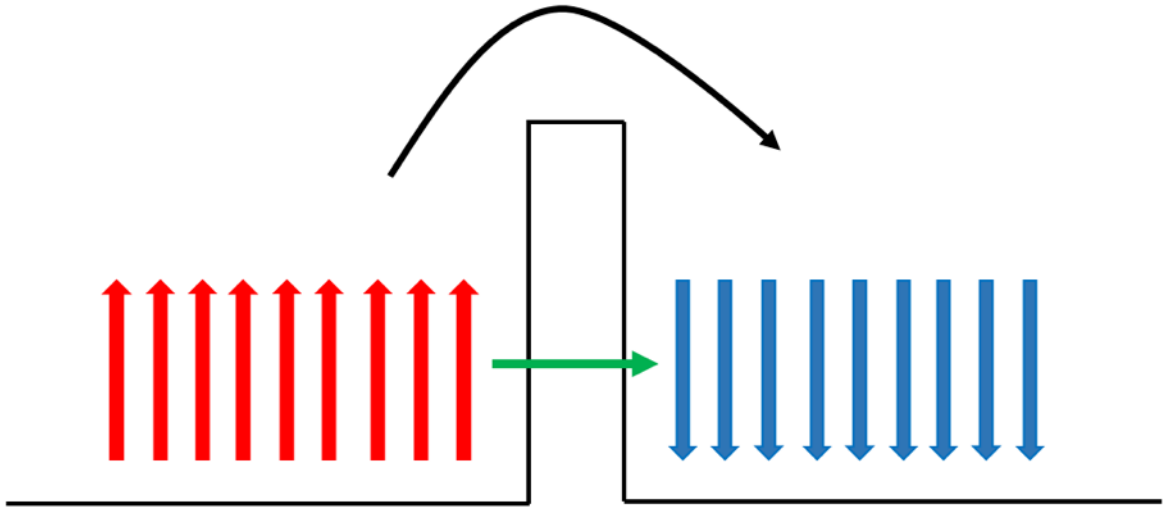

Figure 5.4: Two domain reversal mechanisms. The black arrow shows the classical regime where a domain wall, the effective particle, can only reverse when its energy is higher than the local barriers. In the quantum regime, the particle has a non-zero probability of tunneling through the barrier as a function of the effective mass of the particle.

limits. In the quantum regime the domain walls propagate like a quantum particle where the quantum tunneling rate tunes both the effective mass and the barrier heights. With suitable doping, the quantum magnet $LiHo_xY_{1-x}F_4$ in a transverse field can experience a crossover from the classical pining regime to the quantum speedup regime. Note that in real experiment the effective Γ won't be zero at zero transverse field given the internal dipole fields [62]. That sets the upper limit of the effective mass. The lower limit of the effective mass is when the effective transverse field is comparable with the dipolar interaction. In this case, the system reaches its ferromagnetic-paramagnetic phase boundary when the ferromagnetism becomes unstable. The effective particles can travel freely through the entire system and their effective masses approach zero.

Fig. 5.5 shows the evolution of the hysteresis loops as a function of transverse field in the quantum and classical regimes. In the quantum regime (left), where the hysteresis loop

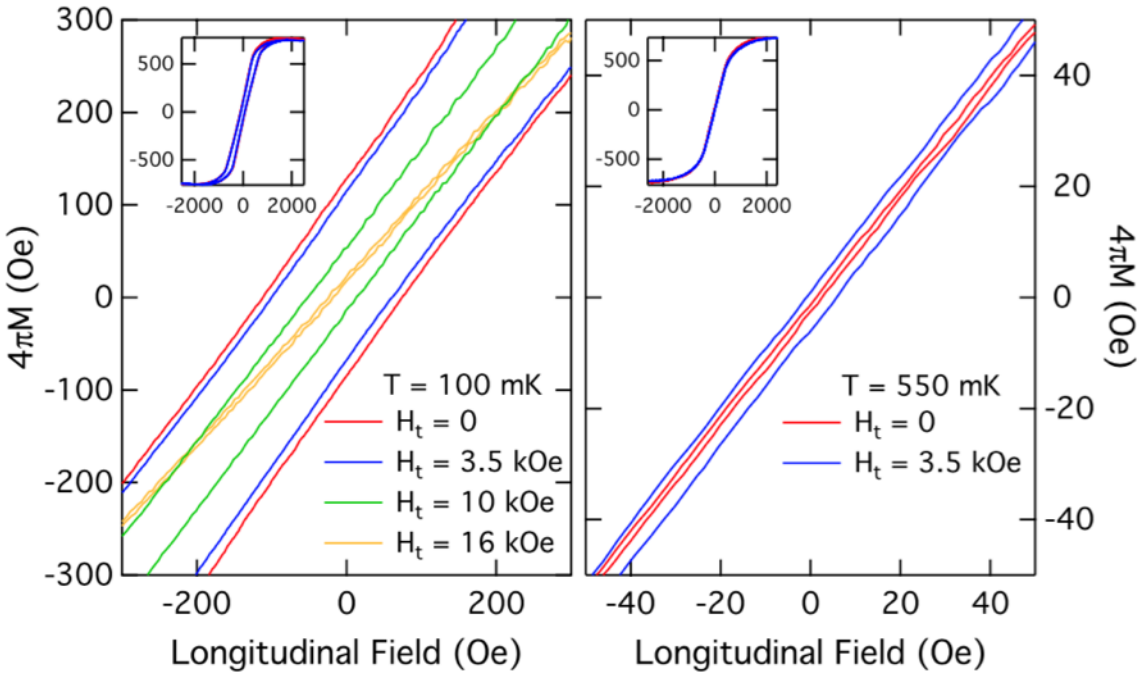

Figure 5.5: Hysteresis loops for $LiHo_{0.44}Y_{0.56}F_4$ sample in the quantum (left) and classical (right) limits. Left panel: The hysteresis loops become narrower as transverse field increases at low temperature. Right panel: the hysteresis loops widens as transverse field increases at high temperature. Insets are full hysteresis loops for the two temperatures. From Ref. [1].

narrows monotonically as transverse field is increased, the domain reversal behavior is clearly not a result of classical domain pinning effect which would harden the ferromagnet and makes the hysteresis loops broader. The narrowness can only be explained by the quantum tunneling mechanism because the quantum tunneling makes it easier for the domain wall to flip at local barrier/pinning centers. Near the Curie temperature, however, the hysteresis loop broadens as transverse field is increased for small transverse field and when transverse field surpasses 3.25 kOe the quantum effect again dominates and narrows the hysteresis loop, as indicated in Fig. 5.6.

The two mechanisms for domain flipping raise interesting questions on how the domain dynamics change as the system sits in different regimes, including whether the system is in a different universality class than mean-field. We know from previous experiments that the characteristic frequency for the weakest pinned domain walls is of order 100 kHz and roughly 10 spins tunnel together [62]. This pushes the limit of our Barkhausen noise apparatus in terms of bandwidth and signal-to-noise ratio (SNR). However, it would be fascinating to see Quantum Barkhausen noise where the reversal mechanism is driven purely by a quantum mechanism.

5.3 Barkhausen noise in the Ising ferromagnet $\mathbf{LiHo_{0.65}Y_{0.35}F_4}$

Crackling noise exists in many natural phenomena and usually exhibits power law behavior over many decades of the size distribution [32, 63, 64]. Two well studied examples are ferromagnets and earthquakes. One of the powerful tools to study potential universality is renormalization group theory [49]. For example, in Barkhausen noise measurements, the distribution of avalanche size S follows distribution $S(T)$ with average size $\langle S(T) \rangle$ for given duration T. Then, for a slightly larger timescale, it should follow that:

$$\langle S(T) \rangle = C \langle S(AT) \rangle \tag{5.2}$$

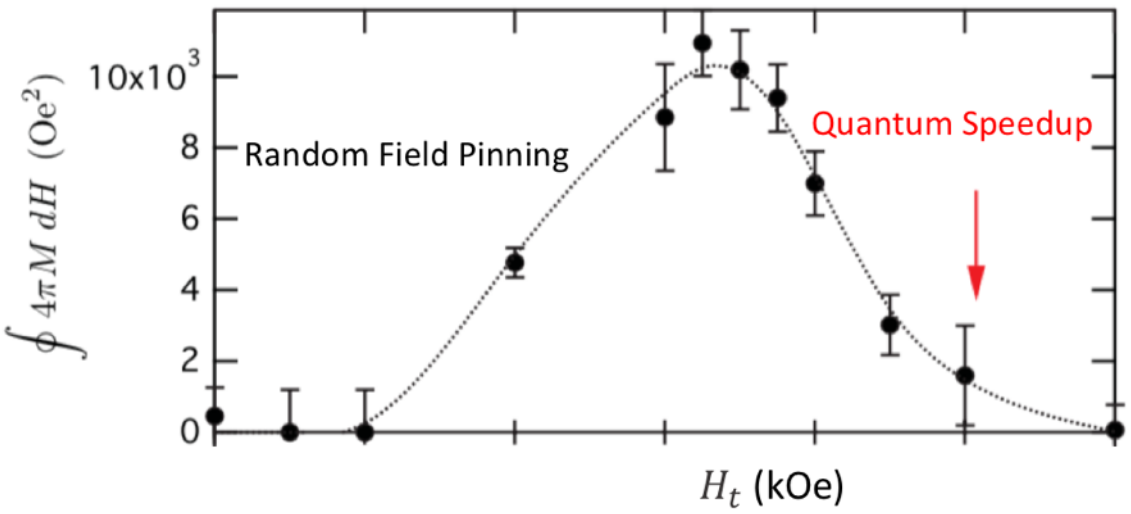

Figure 5.6: The integrated area of the hysteresis loop as a function of transverse field at T = 550 mK. The transverse field tunes the system from classical domain pinning to quantum speedup with a peak at 3.25 kOe. The dashed curve is a guide to the eye. From Ref. [1].

where C, A are scaling factors. If we expand $A = \frac{1}{1-\delta}$ and $C = 1 - a\delta$, then we get the power law equation for size distribution:

$$\langle S(T) \rangle = S_0 T^a \tag{5.3}$$

The exponent a is a critical exponent. However, the self-similarity is not just about the power law distribution. The average shape function is another tool for understanding, as demonstrated by experimental and numerical studies of the average shape of Barkhausen avalanches [32, 49, 63, 65] and earthquakes [64]. Let $\langle V(T,t) \rangle$ be the average line shape for an avalanche of duration T. Universality suggests that $\langle V(T,t) \rangle$ should follow:

$$\langle V(T,t) \rangle = C \langle V(AT,t) \rangle \tag{5.4}$$

Scaling on this equation gives,

$$\langle V(T,t)\rangle = T^a f(t/T) \tag{5.5}$$

Note that the factor $f(t/T)$ is no longer a constant but a function of the time history of average avalanches. Compared to the power law, this scaling form is a much better way to measure the universality because one can always expect a power law distribution for crackling noise but not a universal functional form. If we are able to plot $T^{-a}\langle V(T,t)\rangle$ vs t/T, then we would expect that the average shape of the avalanches would collapse on one curve $f(t/T)$, regardless of the microscopic structure. Note that this assumption would only be valid in the scaling regime. In other words, the system must be near critical disorder R_c and field H_c.

We have collected approximately 1000 events at 8%, 25%, 60% and 70% of the Curie temperature of a $LiHo_{0.65}Y_{0.35}F_4$ sample in zero transverse field, focusing on the bottom of the phase diagram of Fig. 5.3. The size and energy definition is the same as we used for the $Nd_2Fe_{14}B$ data analysis in Chapter 4. To obtain the average line shape, each avalanche is first scaled by its duration T and interpolated onto the desired number of counts, where each count is the resolution of the digitizer. Then the average shape is simply the average of many line shapes over a chosen number of bins.

We plot in Fig. 5.7 and Fig. 5.8 the avalanche size and energy distributions. The ordinate is the probability distribution derived from the average number of events per hysteresis loop divided by the width of the bins on a logarithmic scale. We are only able to fit a good power law to the 700 mK data. The critical exponent of the size distribution, $\tau = 1.5 \pm 0.1$ agrees with the mean-field prediction of 3/2. At lower temperature, however, the tail of the distribution rises up as there are more and more large events. Those large events drive the whole distribution away from a mean-field power law and make it difficult to locate the true scaling regime.

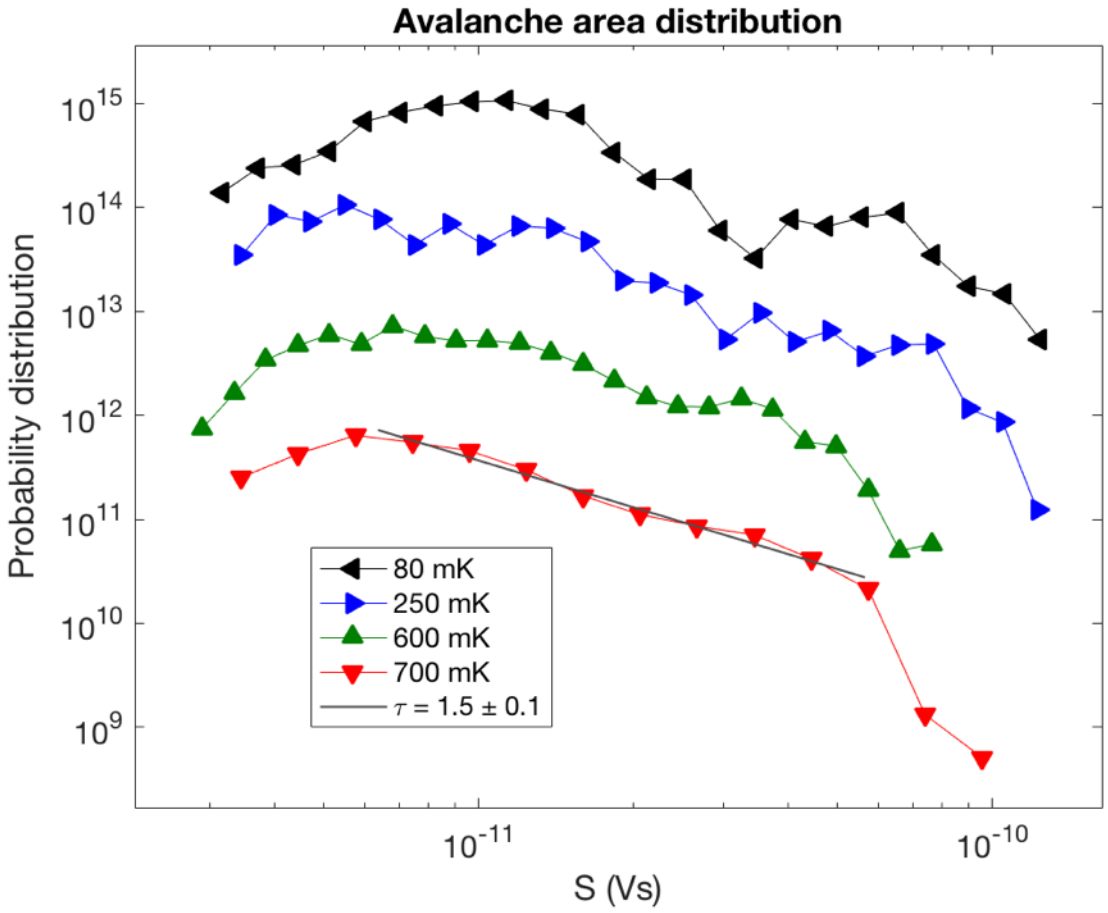

Figure 5.7: Probability distribution of avalanche area at a series of temperatures (80, 250, 600 and 700 mK). The power law fit is best at T = 700 mK, with critical exponent $\tau = 1.5 \pm 0.1$, in agreement with the mean-field prediction, $\tau = \frac{3}{2}$. The increase in the distribution tail indicates more large events happening at lower temperature. Traces for T$\geqslant$250 mK are offset vertically for clarity.

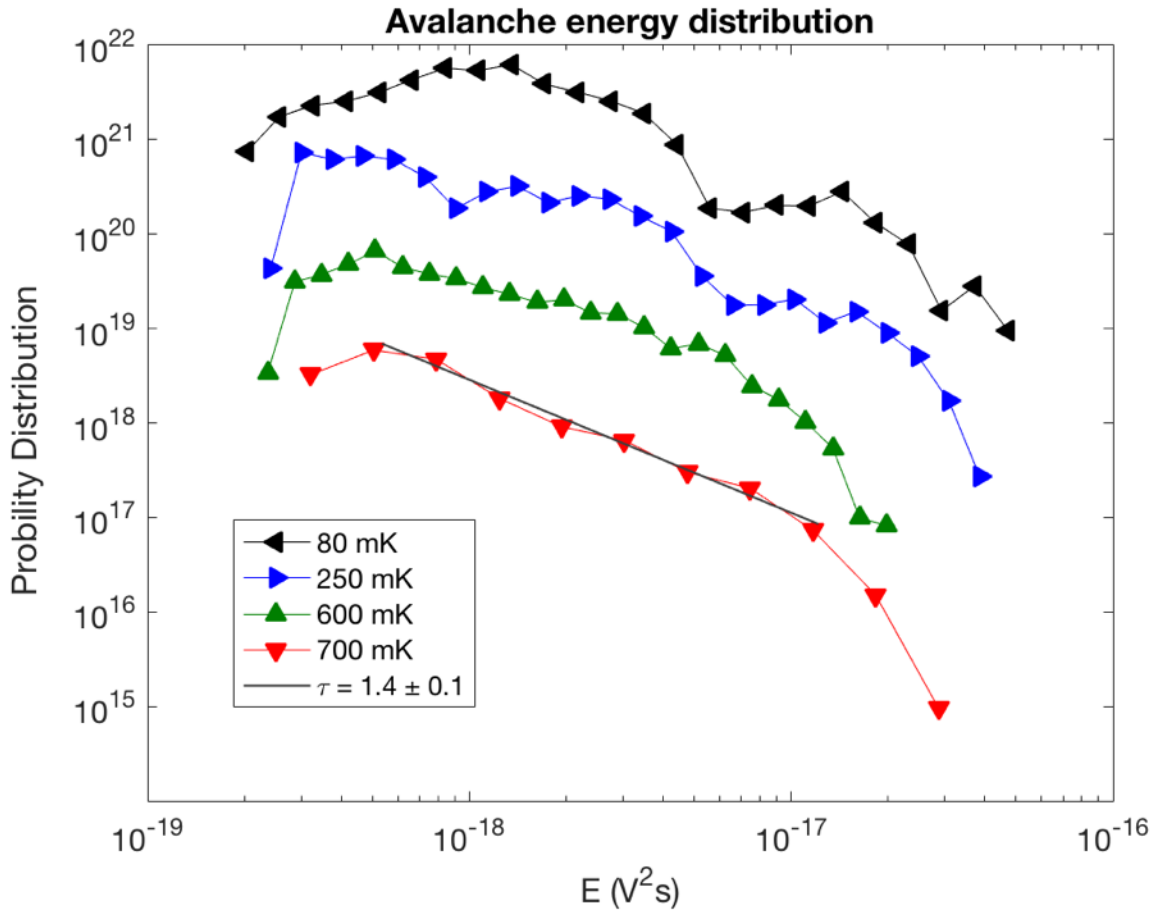

Figure 5.8: Probability distribution of avalanche energy at a series of temperatures T (80, 250, 600 and 700 mK). Power law fit is best at 700 mK, with critical exponent $\tau = 1.4 \pm 0.1$, larger than the mean-field prediction $\tau = \frac{11}{9}$. The increase in the distribution tail indicates more larger events occuring at lower temperature. Traces for T$\geqslant$250 mK are offset vertically for clarity.

The average shape of the avalanche is usually formulated based on the ABBM model [63, 66]. It regards the domain wall position as the single degree of freedom,

$$\beta \dot{X}_t = -ct - kX_t + W(x) \tag{5.6}$$

where β is the damping factor, c is the ramping rate, $-kX_t$ is the demagnetization factor, $W(x)$ is the random field with a Gaussian distribtion and Brownian correlation. Following the assumption in [63], the average shape $\langle V(T, X_t) \rangle$ can be written as:

$$\beta \dot{V}_t = -c - kV_t + \sqrt{2V_t}\xi(t) \tag{5.7}$$

In the limit of $c = 0$ (adiabatic ramping) and zero demagnetization $k = 0$, the average shape can be solved in Stratonovich interpretaion [63]:

$$\langle V(T, t) \rangle = \frac{1}{8} t(1 - \frac{t}{T}) \tag{5.8}$$

where the average shape is an inverse parabola and flatens as duraiton T becomes longer. If the demagnetization factor is non-zero, then,

$$\langle V(T, X_t) \rangle = \frac{1}{2} \frac{(e^{2k(T-t)} - 1)(e^{2kt} - 1)}{e^{2kT} - 1} \tag{5.9}$$

This function will lead to a flatter shape as k decreases. We have shown that the ramp rate is near adiabatic in Chapter 2 and our crystal's geometry is not a pure needle at 10 mm $\times$ 5 mm $\times$ 5 mm. The average shape for a series of binned durations is plotted in Fig. 5.9 - 5.13. The longer the duration T, the narrower the shape becomes. This indicates that the demagnetization factor cannot account fully for the asymmetry that we observe.

The average shape shows strong asymmetry, much like the experimental results of [32, 65]. The explanation offered in the literature for the asymmetry was that the eddy current

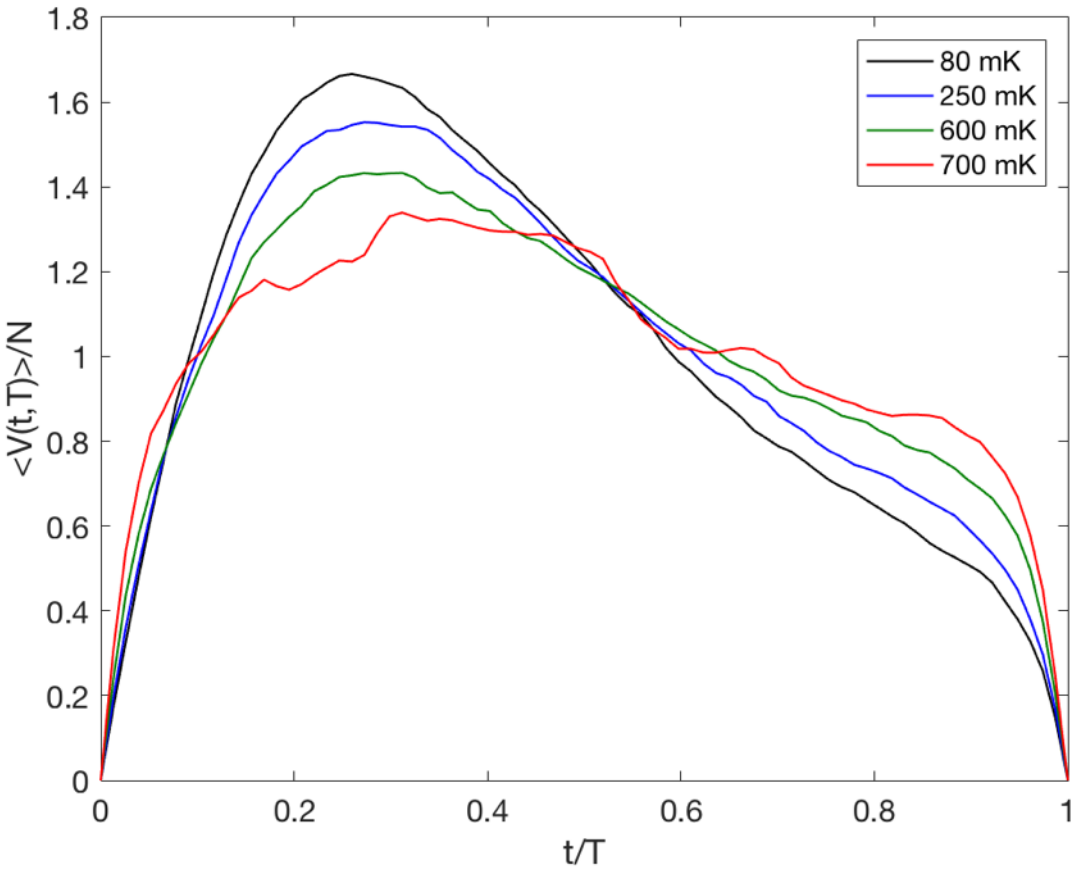

Figure 5.9: The asymmetry of average avalanche shape for a series of temperatures (80, 250, 600, and 700 mK). The normalization factor $N = \int_0^T dt \langle V(T,t) \rangle / T$, where $\langle V(T,t) \rangle$ is the average shape function for duration T.

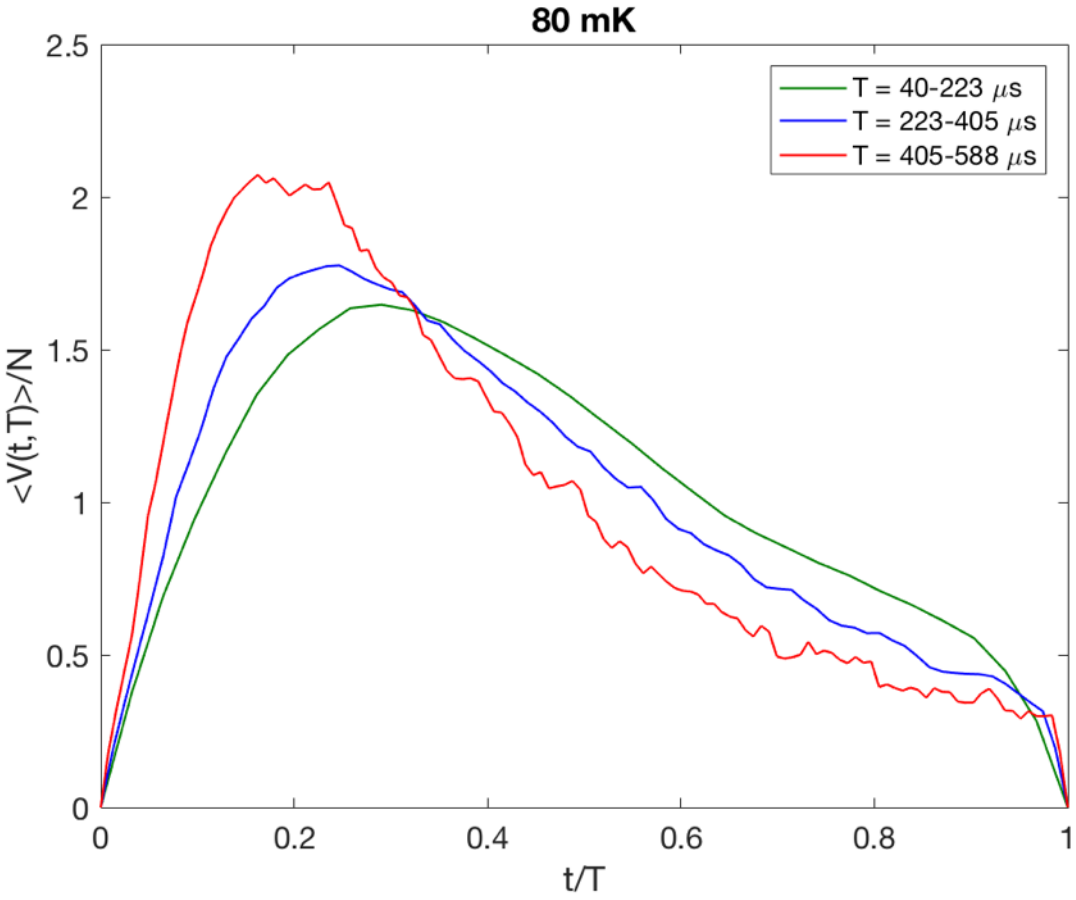

Figure 5.10: The asymmetry of average avalanche shape for binned durations at T = 80 mK.

produced long-range damping term on the right side of Eq. 5.6 so that the eddy current dissipation acted as a drag mechanism for the domain movement. However, our system is a very good insulator with an optical band gap, with no eddy currents. So the revised dynamical equation that they propose doesn't work for this materials. Fig. 5.14 - 5.15 show the average shape for the shortest and longest binned duration. As the duration becomes longer the average shape collapses better onto a universal curve, indicating that domain flips of many spins agree best with the theoretical predictions. This may not be surprising in that any drag effects - although clearly not arising from eddy currents in our system - are less likely to hinder larger avalanches.

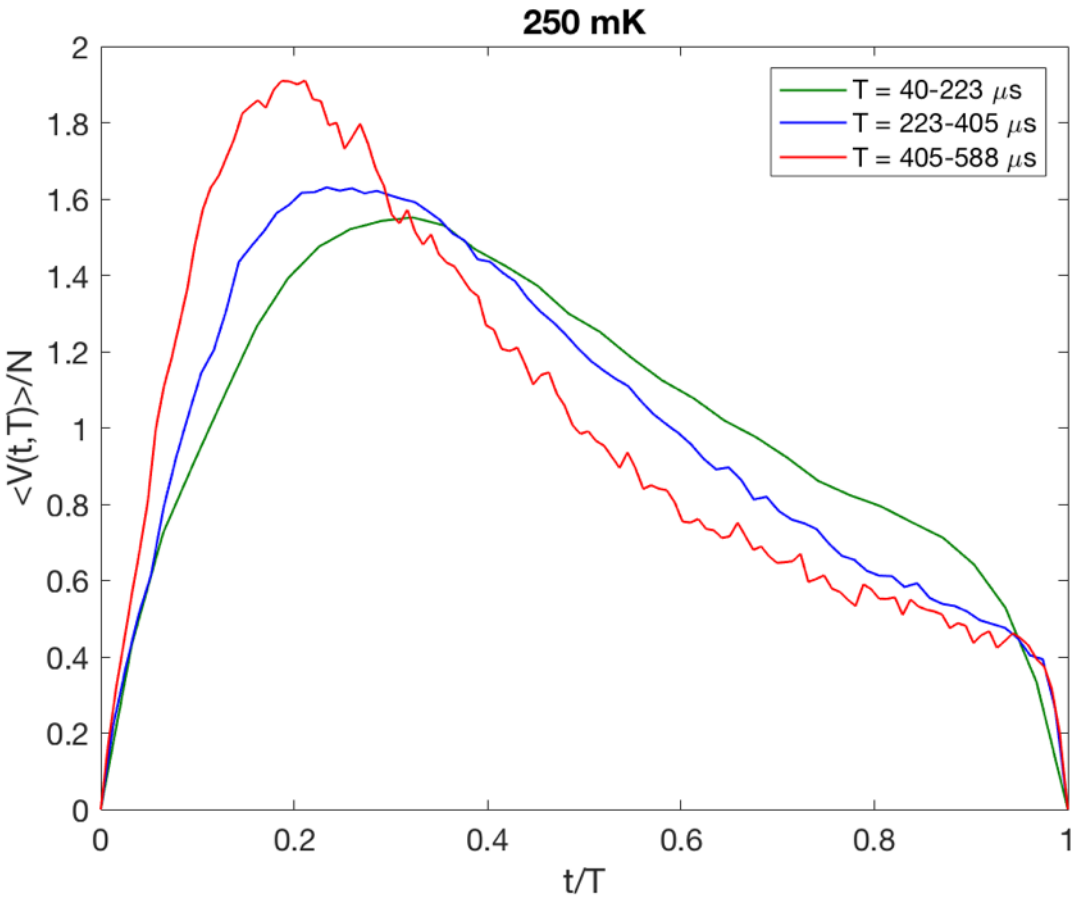

Figure 5.11: The asymmetry of average avalanche shape for binned durations at T = 250 mK.

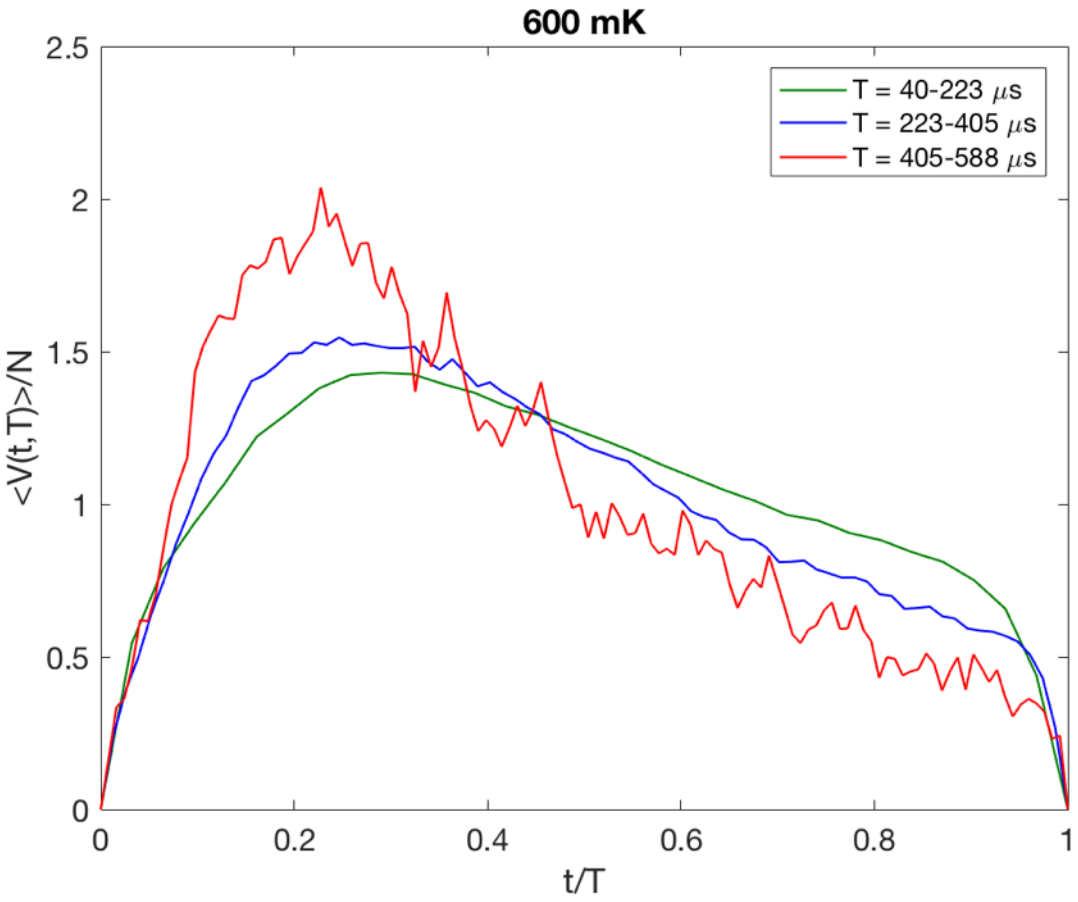

Figure 5.12: The asymmetry of average avalanche shape for binned durations at T = 600 mK.

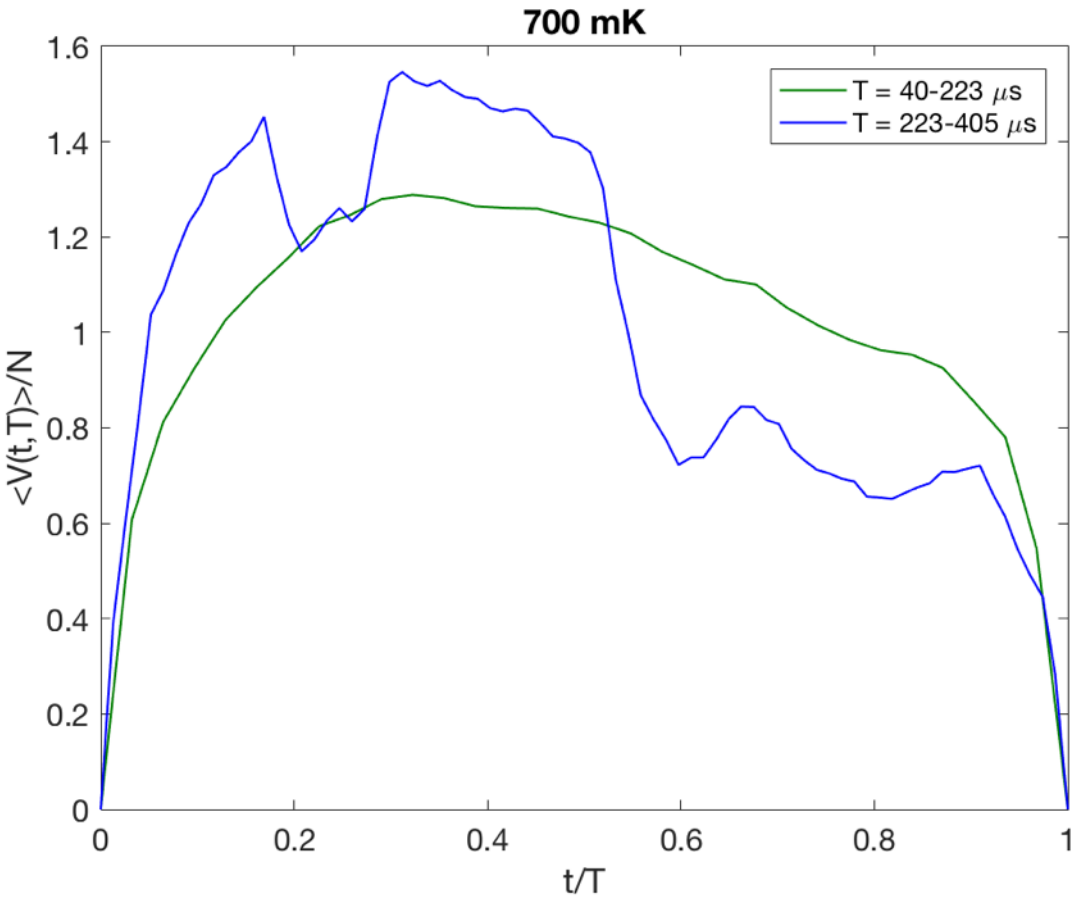

Figure 5.13: The asymmetry of average avalanche shape for binned durations at T = 700 mK.

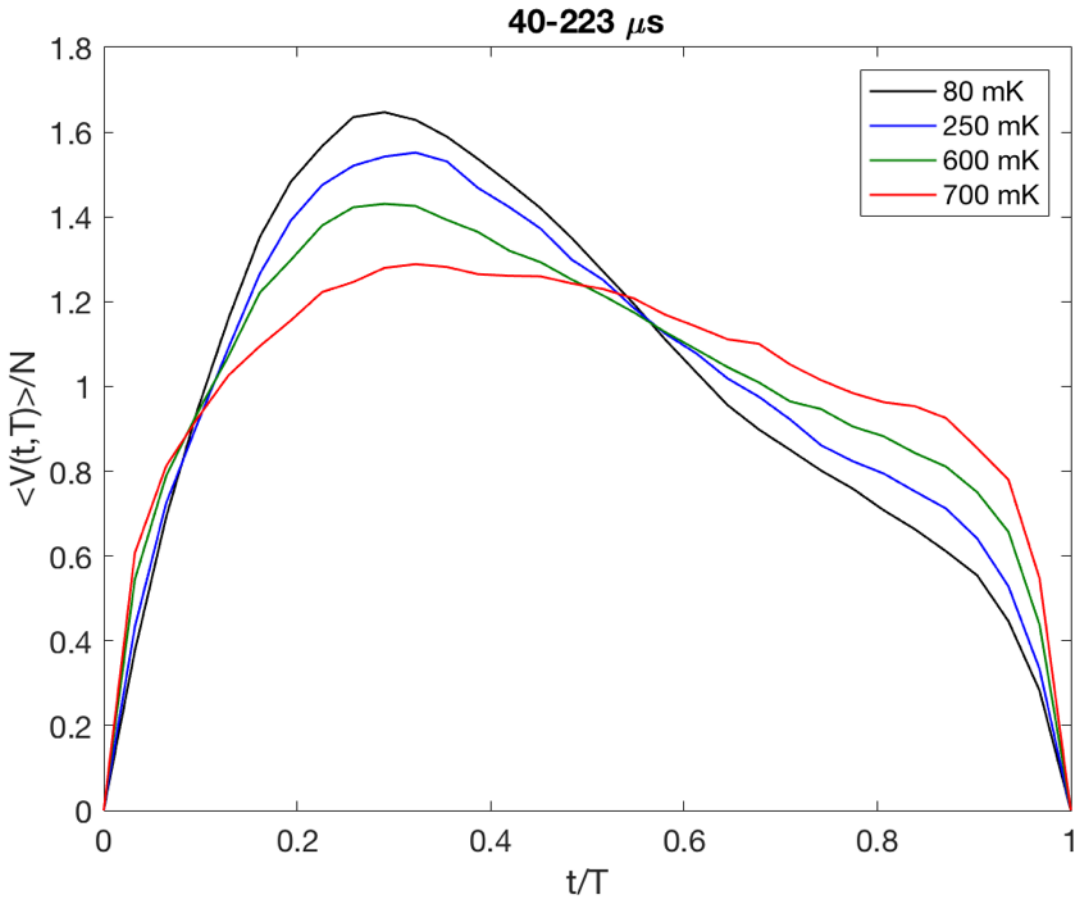

Figure 5.14: Average shape evolution for binned durations between 40−223 μs for a series of temperatures (80, 250, 600, and 700 mK). At the smallest binned duration, the average avalanche shapes don't collapse on top of each other for different temperatures.

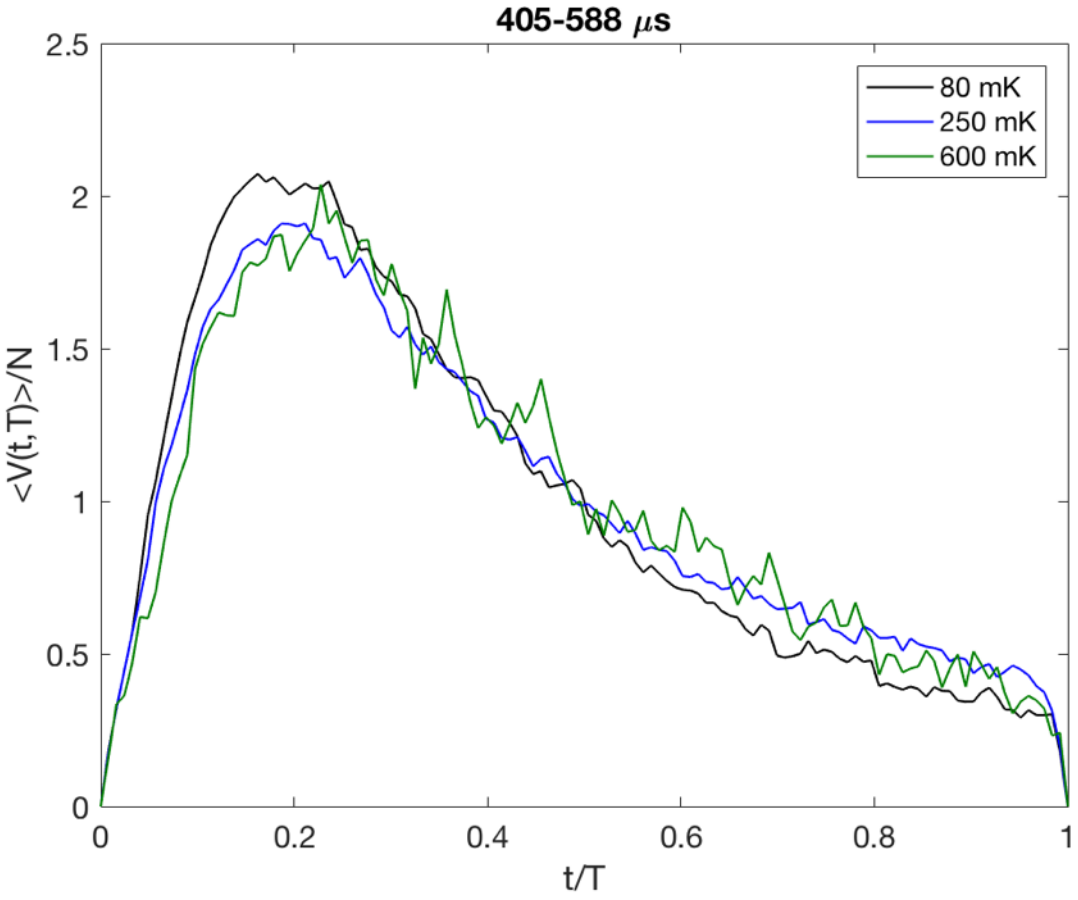

Figure 5.15: Average shape evolution for binned durations between 405−588 μs for a series of temperatures (80, 250, 600, and 700 mK). At the largest binned duration, the average avalanche shapes collapse well on top of each other for different temperatures.

CHAPTER 6

CONCLUSIONS

6.1 Summary of results

The Random field Ising model (RFIM) has been employed successfully as a general model for disordered materials. The dipole-coupled Ising ferromagnet with broken geometric symmetry provides a versatile platform for studying the RFIM. In this thesis, we report the domain dynamics and the critical behavior based on two materials, $Nd_2Fe_{14}B$ and $LiHo_{0.65}Y_{0.35}F_4$, where the former demonstrates Ising ferromagnetism at room temperature and the latter at temperatures below1 K. In both materials, an effective random field is generated as a result of three physical essences: a magnetic field transverse to the Ising axis, the off-diagonal terms in the dipole interaction and symmetry breaking from disorder.

Two papers on $Nd_2Fe_{14}B$ [13, 61] described in this thesis show that uniaxial grains in $Nd_2Fe_{14}B$ serve as effective Ising dipoles and random packing serves as an effective source of symmetry-breaking disorder. The local random field increases the local pinning potential and causes a broadening of the hysteresis loop. By exploring the sub hysteresis loops, we found that the system in the random-field dominated regime will exhibit return point memory (RPM), which is solely a property of a hard magnet. When the transverse field is not applied, the RPM does not hold.

Domain reversal dynamics are studied via the Barkhausen technique. In the disorder-dominated regime, the critical exponents derived from the power law distribution of avalanche size and energy and the scaling collapse of $D(rS^{\sigma}) = \lim_{R \to R_c} S^{\tau+\sigma\beta\delta} D(S, R)$ show that the system is in the mean-field limit. By contrast, in the thermally-dominated regime, the critical exponents and scaling collapse indicate that the system is dominated by fluctuations.

Switchable hardening arising from tunable disorder is possibly applicable to magnetic storage technology. Disorder in bulk materials traditionally can't be tuned easily. For ex-

ample, state-of-the-art magnetic storage materials are Co-based magnetic thin-films. The degree of disorder is controlled by deposition conditions and heat treatment. In most materials, disorder is not reversible. With the effective random field, it is possible to switch the disorder during the write and read process through the simple application of a global magnetic field.

Besides a much smaller energy scale, $LiHo_{0.65}Y_{0.35}F_4$ demonstrates an interesting competition between classical spin pinning and quantum tunneling effects [1]. Due to an improved signal-to-noise ratio, we are able to measurer the far smaller magnetic domains, and we have explored universality beyond scaling power laws. The results raise new questions on what does the average Barkhausen noise look like in the classical and quantum regimes. The average shape function is asymmetric and continuously flattens at higher temperature. Note that $LiHo_{0.65}Y_{0.35}F_4$ is a very good insulator with an optical band gap, so there is no eddy current dragging mechanism to cause that asymmetry, the prevalent claim in the literature from experiments on metallic samples. The demagnetization factor can't fully account for the asymmetry we observe either. Questions remain on what is the dragging mechanism and whether the renormalization group analysis is fundamentally the appropriate approach.

6.2 Future experiments

Barkhausen noise has never been observed from domain reversal caused by quantum tunneling. Would renormalization group (RG) theory describe crackling noise caused by this completely different reversal mechanism? We have shown that even in classical domain reversal with no eddy current drag mechanism, the universal shape function isn't an inverse parabola which is indicated by the RG front propagation and nucleation model [49]. Future experiments which address this fundamental question include:

1. Explore the crossover between classical pinning to quantum tunneling at high temperature, such as 80% of the Curie temperature. It would be especially interesting to see the

evolution of the average shape as a function of transverse field and the universality such as power law exponents and scaling collapse.

2. Explore the full ferromagnetic phase of $LiHo_{0.65}Y_{0.35}F_4$, especially the pure quantum tunneling regime, i.e. at temperatures below 10% of the Curie temperature. We know the characteristic frequency of the quantum tunneling so the Barkhausen noise is expected to be observable as the transverse field is increased.

Another subject to which it would be valuable to apply our techniques would be the two-dimensional dipole-coupled ferromagnet. This is of both theoretical and technological interest. Many thin-film magnetic materials experience strong shape anisotropy effects that cause their magnetic moments to align out of the plane. We can stack many bi-layers of of perpendicular-anisotropy materials such as cobalt with non-magnetic spacers such as platinum [67]. The disorder is controlled by deposition conditions during their growth process. The experiment would then be to probe tunable disorder in these materials via a transverse field and the random field Ising model. The lower dimensionality should increase the fluctuations and noise that we are interested in characterizing.

BIBLIOGRAPHY

[1] D. M. Silevitch, G. Aeppli, and T. F. Rosenbaum. *Proc. Nat. Acad. Sci.*, 107:2797, 2010.

[2] Y. Imry and S.-K. Ma. *Phys. Rev. Lett.*, 35:1399, 1975.

[3] D. P. Belanger, A. R. King, V. Jaccarino, and J. L. Cardy. *Phys. Rev. B*, 28:2522, 1983.

[4] M. Gofman, J. Adler, A. Aharony, A. B. Harris, and M. Schwartz. *J. Appl. Phys.*, 115: 083906, 2014.

[5] H. Yoshizawa, R. A. Cowley, G. Shirane, R. J. Birgeneau, H. J. Guggenheim, and H. Ikeda. *Phys. Rev. Lett.*, 48:438–441, 1982.

[6] W. Kleemann, J. Dec, P. Lehnen, R. Blinc, B. Zalar, and R. Pankrath. *Europhys. Lett.*, 57:14–19, 2002.

[7] T. Granzow, Th. Woike, M. Wöhlecke, M. Imlau, and W. Kleemann. *Phys. Rev. Lett.*, 92:065701, 2004.

[8] S. M. A. Tabei, M. J. P. Gingras, Y.-J. Kao, P. Stasiak, and J.-Y. Fortin. *Phys. Rev. Lett.*, 97:237203, 2006.

[9] M. Schechter. *Phys. Rev. B*, 77:020401, 2008.

[10] A. J. Millis, A. D. Kent, M. P. Sarachik, and Y. Yeshurun. *Phys. Rev. B*, 81:024423, 2010.

[11] D. M. Silevitch, D. Bitko, J. Brooke, S. Ghosh, G. Aeppli, and T. F. Rosenbaum. *Nature*, 448:567, 2007.

[12] B. Wen, P. Subedi, Lin Bo, Y. Yeshurun, M. P. Sarachik, A. D. Kent, A. J. Millis, C. Lampropoulos, and G. Christou. *Phys. Rev. B*, 82:014406, 2010.

[13] S. L. Tomarken, D. M. Silevitch, G. Aeppli, B. A.W. Brinkman, J. Xu, K. A. Dahmen, and T. F. Rosenbaum. *Adv. Funct. Mater.*, 24:2986, 2014.

[14] D. Givord, H. S. Li, and R. Perrier de la Bâthie. *Solid State Comm.*, 51:857, 1984.

[15] J. F. Herbst, J. J. Croat, F. E. Pinkerton, and W. B. Yelon. *Phys. Rev. B*, 29:4176–4178, 1984.

[16] K.-D. Durst and H. Kronmu̇ller. *J. Magn. Magn. Mater.*, 68:63–75, 1987.

[17] J. F. Herbst. *Rev. Mod. Phys.*, 63:819–898, 1991.

[18] M. S. Pierce, C. R. Buechler, L. B. Sorensen, J. J. Turner, S. D. Kevan, E. A. Jagla, J. M. Deutsch, T. Mai, O. Narayan, J. E. Davies, K. Liu, J. Hunter Dunn, K. M. Chesnel, J. B. Kortright, O. Hellwig, and E. E. Fullerton. *Phys. Rev. Lett.*, 94:017202, 2005.

[19] M. S. Pierce, C. R. Buechler, L. B. Sorensen, S. D. Kevan, E. A. Jagla, J. M. Deutsch, T. Mai, O. Narayan, J. E. Davies, K. Liu, G. T. Zimanyi, H. G. Katzgraber, O. Hellwig, E. E. Fullerton, P. Fischer, and J. B. Kortright. *Phys. Rev. B*, 75:144406, 2007.

[20] O. Hellwig, A. Berger, J. B. Kortright, and E. E. Fullerton. *J. Magn. Magn. Mater.*, 319:13, 2007.

[21] S. Fishman and A. Aharony. *J. Phys. C: Solid State Phys.*, 12:L729, 1979.

[22] E. Pytte, Y. Imry, and D. Mukamel. *Phys. Rev. Lett.*, 46:1173, 1981.

[23] A. J. Bray and M. A. Moore. *J. Phys. C: Solid State Phys.*, 18:L927, 1985.

[24] G. Mennenga, L.J. de Jongh, and W.J.Huiskamp. *J. Magn. Magn. Mater.*, 44:59–76, 1983.

[25] W. H. Wu, B. Ellman, T. F. Rosenbaum, G. Aeppli, and D. H. Reich. *Phys. Rev. Lett.*, 67:2076–2079, 1991.

[26] D. Bitko, T. F. Rosenbaum, and G. Aeppli. *Phys. Rev. Lett.*, 77:940–943, 1996.

[27] P. B. Chakraborty, P. Henelius, H. Kjønsberg, A. W. Sandvik, and S. M. Girvin. *Phys. Rev. B*, 70:144411, 2004.

[28] A. Biltmo and P. Henelius. *Phys. Rev. B*, 78:054437, 2008.

[29] J. Brooke. *Ph.D. thesis, Department of Physics*, 2000.

[30] H. Barkhausen. *Phys. Z.*, 20:401, 1919.

[31] O. Kypris I. C. Nlebedim and D. C. Jiles. *J. Appl. Phys.*, 115:083906, 2014.

[32] D. Spasojević, S. Bukvić, S. Milošević, and H. E. Stanley. *Phys. Rev. E*, 54:2531–2546, 1996.

[33] H. Yoshizawa, R. A. Cowley, G. Shirane, and R. Birgeneau. *Phys. Rev. B*, 31:4548–4556, 1985.

[34] T. Nattermann and I. Vilfan. *Phys. Rev. Lett.*, 61:223–226, 1988.

[35] R. Bruinsma and G. Aeppli. *Phys. Rev. Lett.*, 52:1547–1550, 1984.

[36] A. Hutten. *JOM*, 44:11, 1992.

[37] D. Weller, A. Moser, L. Folks, M. E. Best, W. Lee, M. F. Toney, M. Schwickert, J. U. Thiele, and M. F. Doerner. *IEEE Trans. Magn.*, 36:10, 2000.

[38] G. Ayton, M. J. P. Gingras, and G. N. Patey. *Phys. Rev. E*, 56:562–570, 1997.

[39] T. Miyazaki and H. Jin. *The Physics of Ferromagnetism, Springer-Verlag, Berlin, Germany*, page 100, 2012.

[40] J. M. D. Coey and K. ODonnell. *J. Appl. Phys.*, 81:4810, 1997.

[41] D. A. Huse and C. L. Henley. *Phys. Rev. Lett.*, 54:2708–2711, 1985.

[42] J. D. Livingston. *J. Appl. Phys.*, 52:2544, 1981.

[43] D. M. Silevitch, T. F. Rosenbaum, and G. Aeppli. *U.S. Patent 8,558,333; EU Patent Application 10797895.9EPO*, 2013.

[44] J. P. Sethna. *Phys. Rev. Lett.*, 70:3347, 1993.

[45] K. P. O'Brien and M. B. Weissman. *Phys. Rev. E*, 50:3446–3452, 1994.

[46] P. Plewka, J. J. Żebrowski, and M. Urbański. *Phys. Rev. E*, 57:6422–6431, 1998.

[47] S. Zapperi, P. Cizeau, G. Durin, and H. E. Stanley. *Phys. Rev. B*, 58:6353–6366, 1998.

[48] G. Durin and S. Zapperi. *Phys. Rev. Lett.*, 84:4705–4708, 2000.

[49] J. P. Sethna, K. A. Dahmen, and C. R. Myers. *Nature*, 410:242, 2001.

[50] T. Schrefl, H. Roitner, and J. Fidlser. *J. Appl. Phys.*, 81:5567, 1997.

[51] F. J. Pérez-Reche, B. Tadić, L. Mañosa, A. Planes, and E. Vives. *Phys. Rev. Lett.*, 93: 195701, 2004.

[52] E. Vives and A. Planes. *Phys. Rev. B*, 63:134431, 2001.

[53] R. Alben, J. J. Becker, and M. C. Chi. *J. Appl. Phys.*, 49:1653–1658, 1978.

[54] O. Perković, K. A. Dahmen, and J. P. Sethna. *Phys. Rev. B*, 59:6106–6119, 1999.

[55] D. H. Reich, B. Ellman, J. Yang, T. F. Rosenbaum, G. Aeppli, and D. P. Belanger. *Phys. Rev. B*, 42:4631–4644, 1990.

[56] P. E. Hansen, T. Johansson, and R. Nevald. *Phys. Rev. B*, 12:5315–5324, 1975.

[57] K. J. Knak Jensen and K. Kjaer. *J. Phys. Condens. Matter*, 1:2361, 1989.

[58] C. Ancona-Torres, D. M. Silevitch, G. Aeppli, and T. F. Rosenbaum. *Phys. Rev. Lett.*, 101:057201, 2008.

[59] M. Suzuki. *Prog. Theor. Phys.*, 56:1454, 1976.

[60] J. Oitmaa and G. J. Coombs. *J. Phys. C*, 14:143, 1981.

[61] J. Xu, D. M. Silevitch, K. A. Dahmen, and T. F. Rosenbaum. *Phys. Rev. B*, 92:024424, 2015.

[62] J. Brooke, T. F. Rosenbaum, and G. Aeppli. *Nature*, 413:610–613, 2001.

[63] S. Papanikolaou, F. Bohn, R. L. Sommer, G. Durin, S. Zapperi, and J. P. Sethna. *Nat. Phys.*, 7:316–320, 2011.

[64] A. P. Mehta, K. A. Dahmen, and Y. Ben-Zion. *Phys. Rev. E*, 73:056104, 2006.

[65] S. Zapperi, C. Castellano, Fr. Colaiori, and G. Durin. *Nat. Phys.*, 1:46–49, 2005.

[66] B. Alessandro, C. Beatrice, G. Bertotti, and Montorsi A. *J. Appl. Phys.*, 68:2901–2907, 1990.

[67] K. Takano, G. Zeltzer, D.K. Weller, and E.E. Fullerton. *J. Appl. Phys.*, 87:6364, 2000.